

Seismological Characterization of the 2021 Yangbi Foreshock-Mainshock Sequence, Yunnan, China: More than a Triggered Cascade

Yijian Zhou¹, Chunmei Ren², Abhijit Ghosh³, Haoran Meng⁴, Lihua Fang⁵, Han Yue⁶,
Shiyong Zhou⁶, and Youjin Su⁷

¹Department of Earth and Planetary Sciences, University of California Riverside

²Institute of Theoretical and Applied Geophysics

³University of California, Riverside

⁴Southern University of Science and Technology

⁵Institute of Geophysics, China Earthquake Administration

⁶Peking University

⁷Yunnan Earthquake Agency

November 26, 2022

Abstract

The 2021 M_w 6.1 Yangbi earthquake in southwest China is preceded by three major foreshocks: 05/18 M_w 4.3, 05/19 M_w 4.6, and 05/21 M_w 5.2. It provides a valuable chance to revisit two end-member models describing earthquake interaction: cascade-up and pre-slip model. We first determine the associated fault structure with relocated aftershocks and focal mechanisms obtained from multi-point-source inversion. We find that the mainshock and two smaller foreshocks occur on an unmapped near-vertical fault, and the largest foreshock occurs on a mapped stepover fault that dips to NE. Secondly, for each major foreshock, we estimate and delineate their rupture area based on aftershocks and spectral ratio analysis. Based on the rupture model, we finally calculate the evolution of Coulomb stress, with which to interpret the causality of each major event. Results show that the Yangbi sequence can be explained by the cascade triggering mechanism, while we also find evidence for aseismic slip that contributes to the triggering process: the first foreshock is preceded by a short-term localized cluster, and the aftershock zone of the second foreshock extends through time. The nucleation of mainshock is probably contributed by multiple major foreshocks through both seismic and aseismic processes. This detailed seismological characterization of Yangbi sequence lend supports for a deeper understanding on the foreshock mechanism: (1) the controlling mechanisms are not limited to cascade-up & pre-slip, multiple mechanisms can operate together; and (2) aseismic slip does not always provide more predictability on the mainshock.

1 **Seismological Characterization of the 2021 Yangbi Foreshock-Mainshock**
2 **Sequence, Yunnan, China: More than a Triggered Cascade**

3
4 **Yijian Zhou^{1*}, Chunmei Ren², Abhijit Ghosh¹, Haoran Meng³, Lihua Fang^{4*}, Han Yue²,**
5 **Shiyong Zhou², Youjin Su⁵**

6 ¹Department of Earth and Planetary Sciences, University of California, Riverside, California, USA

7 ²Institute of Theoretical and Applied Geophysics, Peking University, Beijing, China.

8 ³Southern University of Science and Technology, Guangdong, China

9 ⁴Institute of Geophysics, China Earthquake Administration, Beijing, China

10 ⁵Yunnan Earthquake Agency, Yunnan, China

11
12 Corresponding author:

13 Yijian Zhou (yijian.zhou@email.ucr.edu)

14 Lihua Fang (flh@cea-igp.ac.cn)

15 **Key Points:**

- 16 • The Yangbi mainshock and two smaller foreshocks occur on an unmapped near-vertical
17 fault, and the largest foreshock occurs on a mapped stepover fault that dips to NE.
- 18 • The rupture directivity and source parameters of major foreshocks are estimated by
19 aftershock distribution and spectral ratio analysis.
- 20 • The Yangbi sequence can be explained as a cascade sequence, but aseismic signals are also
21 detected, including pre-slip cluster and afterslip migration.
- 22

23 **Abstract**

24 The 2021 M_w 6.1 Yangbi earthquake in southwest China is preceded by three major
25 foreshocks: 05/18 M_w 4.3, 05/19 M_w 4.6, and 05/21 M_w 5.2. It provides a valuable chance to revisit
26 two end-member models describing earthquake interaction: cascade-up and pre-slip model. We
27 first determine the associated fault structure with relocated aftershocks and focal mechanisms
28 obtained from multi-point-source inversion. We find that the mainshock and two smaller
29 foreshocks occur on an unmapped near-vertical fault, and the largest foreshock occurs on a mapped
30 stepover fault that dips to NE. Secondly, for each major foreshock, we estimate and delineate their
31 rupture area based on aftershocks and spectral ratio analysis. Based on the rupture model, we
32 finally calculate the evolution of Coulomb stress, with which to interpret the causality of each
33 major event. Results show that the Yangbi sequence can be explained by the cascade triggering
34 mechanism, while we also find evidence for aseismic slip that contributes to the triggering process:
35 the first foreshock is preceded by a short-term localized cluster, and the aftershock zone of the
36 second foreshock extends through time. The nucleation of mainshock is probably contributed by
37 multiple major foreshocks through both seismic and aseismic processes. This detailed
38 seismological characterization of Yangbi sequence lend supports for a deeper understanding on
39 the foreshock mechanism: (1) the controlling mechanisms are not limited to cascade-up & pre-slip,
40 multiple mechanisms can operate together; and (2) aseismic slip does not always provide more
41 predictability on the mainshock.

42 **Plain Language Summary**

43 The 2021 M_w 6.1 Yangbi earthquake is preceded by three M 4-5 earthquakes, which are
44 known as foreshocks. Whether the foreshock sequence can lend predictability to the mainshock is
45 of scientific interest. For the Yangbi foreshock sequence, we analyze the interaction between the
46 major foreshocks with a high-resolution seismic catalog and the modeling of resulted stress
47 transfer after each major foreshock. Results show that the Yangbi foreshock sequence is not helpful
48 in the prediction of mainshock, but it deepens our understanding toward the phenomenon of
49 foreshocks.

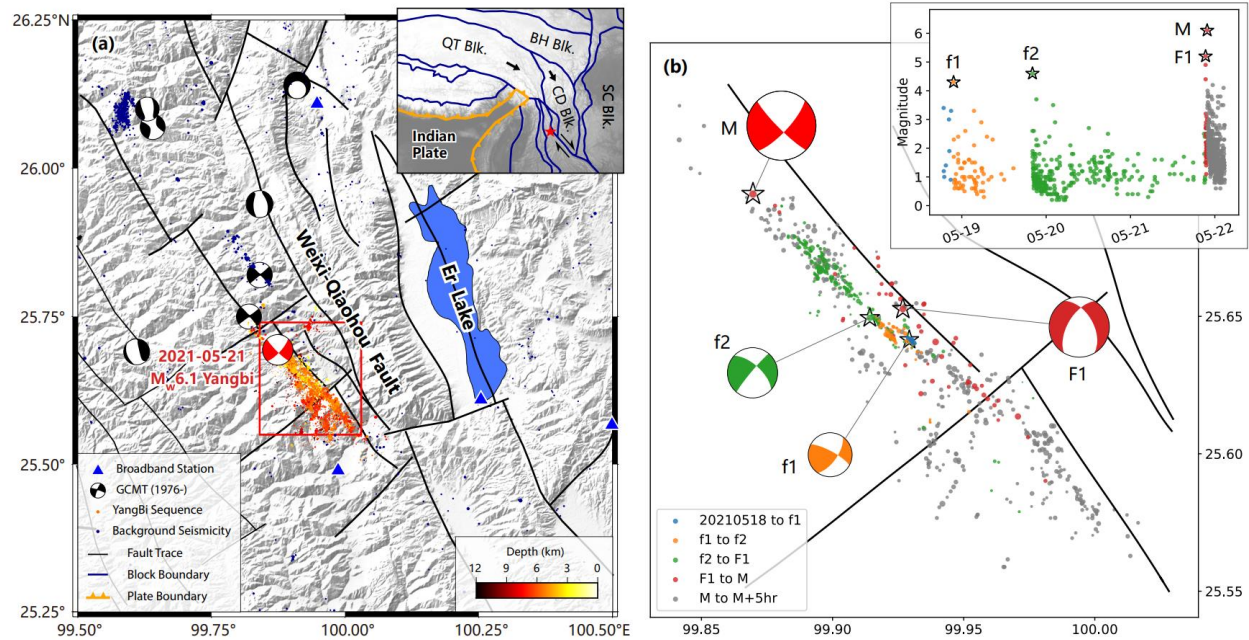
50 1. Introduction

51 Foreshocks are known as smaller earthquakes preceding the large mainshock (Jones and
52 Molnar, 1979). Due to the neighboring location and temporal correlation, foreshocks are
53 considered as a possible precursory phenomenon, e.g. the success prediction of 1975 M_w 7.0
54 Haicheng earthquake largely relies on the \sim 1-day foreshock activity (Wang et al., 2006).
55 Traditionally, two end-member models are proposed to explain the triggering relationship between
56 the foreshocks and mainshock (Dodge et al., 1996): the cascade model and the pre-slip model. The
57 cascade model describes the seismic sequence as the cascade failure of isolated asperities, where
58 each event is triggered by the stress transfer from the previous earthquake (Helmstetter et al., 2003;
59 Felzer et al., 2004; Ellsworth and Bulut, 2018; Yoon et al., 2019). Thus, the initiation process of
60 mainshock and foreshocks are identical, which lead to an unpredictable nature of the mainshock.
61 On the other end, the pre-slip model regards the foreshocks as the byproduct of the nucleation
62 process of the mainshock, where accelerating aseismic slip is accompanied. It is a deterministic
63 model, because theoretical and laboratory studies have shown that the nucleation size, i.e. the area
64 of pre-slip, scales with the final size of the mainshock (Dieterich, 1978; 1992; Ampuero and Rubin,
65 2008; Johnson et al., 2013). The different implications for earthquake predictability make it
66 important to discriminate between different foreshock-mainshock triggering mechanisms.

67 The 2021 M_w 6.1 Yangbi earthquake that strikes the Yunnan province of southwest China
68 is a typical large earthquake with prominent foreshock activity (Figure 1). It occurs near the
69 southwestern boundary of Chuandian block (Zhang et al., 2003) dominated by right-lateral strike-
70 slip motion (Shen et al., 2005). The aftershock of Yangbi earthquake reveals an NW-SE trending
71 fault that is subparallel with the major active fault, i.e. Weixi-Qiaohou fault (Figure 1a). The
72 Yangbi sequence is composed of the 21st May M_w 6.1 mainshock (denoted as M) and three major
73 foreshocks (Figure 1b): the 18th May M_w 4.3 ($f1$), the 19th May M_w 4.6 ($f2$), and the 21st May M_w
74 5.2 earthquake ($F1$). Moment tensor inversion results in right-lateral focal mechanism for these
75 four events (Yang et al., 2021), which is also consistent with the major fault trend. The foreshocks
76 are located in the middle of the mainshock co-seismic fault segment, all of which show clear
77 unilateral rupture, indicated by the relative location between the epicenter and their aftershocks
78 (Figure 1b): $f1$ and $f2$ rupture to northwest, while $F1$ mainly rupture to southeast with certain
79 bilateral component.

80 Up to date, a few discussions are published on the triggering relation between those major
81 foreshocks and the Yangbi mainshock, but no consistent conclusions are reached (e.g., Lei et al.,
82 2021; Zhang et al., 2021; Liu et al., 2022; Sun et al., 2022). It is not surprising, since the
83 conclusions on foreshock formation can vary by different analysis techniques and data conditions
84 (Mignan, 2014). As an example, Ellsworth and Bulut (2018) made detailed event relocation and
85 source spectra analysis to investigate the inter-event triggering effect of the 1999 Izmit foreshocks,
86 which turned out to be a cascading sequence, instead of precursory aseismic slip loading proposed
87 by Bouchon et al. (2011). Thus, the modeling of Coulomb stress with well-constraint event
88 location and finite faulting model is necessary in such discussions. Fortunately, the rather dense
89 regional seismic network in the Yunnan province of China made such analysis possible in Yangbi.
90 Such well-recorded continental large earthquake with intense foreshock activity is rare, and thus
91 provides a valuable chance to generate a well-depicted case for the seismological community.
92 Moreover, the Yangbi earthquake is the largest event that occurs in southwest Chuandian block
93 since the 1996 M_w 6.6 Lijiang earthquake (Han et al., 2004; Ji et al., 2017) and is the largest
94 earthquake in China that has clear foreshock activity since the 1975 M_w 7.0 Haicheng earthquake
95 (Xu et al., 1982; Wang et al., 2006). Thus, an in-depth study in the Yangbi sequence has
96 implications on not only the foreshock mechanism and the seismic hazard of southwest China.

97 In this study, we follow a similar strategy as Ellsworth and Bulut (2018), but focus on
98 larger events with finite source and rupture directivity, to investigate the triggering mechanism of
99 Yangbi sequence. We first determine the local fault structure based on the rupture directivity,
100 aftershock distribution, and the focal mechanism. Secondly, we delineate the finite rupture area
101 for each major foreshock based on aftershocks and spectral ratio analysis. Finally, we model the
102 evolution of Coulomb stress, based on which we interpret the causality of each major event.



103
 104 **Figure 1.** Tectonic background and foreshock sequence. (a) Tectonic background of the Yangbi
 105 earthquake. In the main plot, fault traces are plotted by black lines, and come from Wang et al. (2021). The
 106 interseismic background seismicity and Yangbi seismic sequence are plotted by blue and orange dots
 107 respectively, with the focal depth color-coded. Focal mechanism of GCMT since 1976 is plotted by black
 108 beachballs. Blue triangles mark the broadband stations. In the insert plot, the plate boundary and active
 109 block boundary are plotted by orange and blue lines, respectively. Main blocks, i.e. Qiangtang block (QT),
 110 Bayan Har block (BH), Chuandian block (CD), and South China block (SC), are noted, with their relative
 111 motion marked. (b) The Yangbi foreshock sequence. The study time period is divided by the major
 112 foreshocks ($f1$, $f2$, and $F1$) and the mainshock (M). Seismic catalog comes from Zhou et al. (2021a). The
 113 focal mechanisms of the mainshock and largest foreshocks are determined by multi-point-source inversion,
 114 and that of the first two smaller foreshocks comes from Yang et al. (2021).

115 2. Data and Methods

116 2.1 Seismic Catalog

117 We adopt a high-resolution seismic catalog constructed by Zhou et al. (2021a) with deep
 118 learning and matched filter. The catalog contains 7943 well-located events in the Yangbi source
 119 region from 2021-05-01 to 2021-05-28, which covers the foreshock and early-aftershock period
 120 that is interested in this study. The construction of this catalog utilized an AI-based phase picker
 121 to obtain the template catalog (Zhou et al., 2019) and matched filter to augment the templates
 122 (Zhou et al., 2021b). Such strategy gives reliable and highly complete detection, and thus the

123 catalog reaches a complete magnitude of M_L 1.0, and a minimum magnitude of M_L -1.0. The
124 relocation process utilized cross-correlated differential travel times, which provides sub-sampling-
125 rate precision (<0.01 -s), leading to a relative location uncertainty of ~ 10 m laterally and ~ 20 m
126 vertically in the hypoDD inversion process (Waldhauser, 2001; Zhou et al., 2021a).

127 **2.2 Spectral Ratio Analysis**

128 We use a spectral ratio method to extract the source spectrum of the Yangbi foreshocks, in
129 the purpose of determining their rupture directivity and source parameters. This method utilizes
130 empirical Green's function (EGF) to remove the wave propagation effect and site response in the
131 target foreshock seismogram (Chen and Shearer, 2013; Ross and Ben-Zion, 2016; Ellsworth and
132 Bulut, 2018; Yoon et al., 2019). EGFs are selected as smaller events (usually >1 magnitude smaller)
133 that occur near the target event, so that they can be considered as point source and share similar
134 ray paths with the target event. Thus, on the same station, the ratio between target and EGF spectra
135 represents the source spectrum of target event, which contains the seismic source information, e.g.
136 rupture area, coseismic slip, stress drop, etc. In the Yangbi sequence, we select the aftershocks of
137 the target foreshock as EGF, which is both large enough to be clearly recorded on selected stations,
138 and small enough to be considered as a point source. This leads to 6 to 10 EGFs with the magnitude
139 range from M_L 2.6-3.5 for $f1$ and $f2$, and M_L 2.9-4.1 for $F1$.

140 The rupture directivity can be revealed by the azimuthal variation of source spectrum
141 (Calderoni et al., 2015; Calderoni et al., 2017). Based on the dynamic rupture theory, stations
142 facing the rupture propagation direction are expected to observe a source-time function (STF) of
143 shorter duration and higher amplitude; or, in the frequency domain, a higher corner frequency on
144 the source spectrum (Haskell, 1964). Thus, we apply two sets of comparison on the source
145 spectrum observed on two sides of the target earthquake: one set along fault-parallel direction and
146 another along fault-normal direction. For unilateral rupture, the contrast of corner frequency along
147 fault-parallel would be larger than the fault-normal one; for bilateral rupture, both directions have
148 weak contrasts, but fault-parallel stations would record larger high-frequency components.

149 For the estimation of rupture area, we use fault-normal stations to obtain the corner
150 frequency that has little directivity effect. We calculate the S-wave spectrum with a multi-taper
151 algorithm (Prieto et al., 2009), and normalize it by its seismic moment (Ross and Ben-Zion, 2016).
152 We adopt several strategies to improve the stability of spectral ratio calculation: (1) the initial

153 result is smoothed in log-scale by interpolation and sampling on every 0.025 of log(f); (2) for each
 154 event-station pair, we utilize a multi-window strategy (Imanishi and Ellsworth, 2006; Uchida et
 155 al., 2007; Yoon et al., 2019): three 10-s sliding windows with a 1.5-s stride are applied, where the
 156 first window starts from the S wave arrival. The spectrum of these sliding windows is averaged on
 157 the log scale; (3) the spectrum of different EGFs are stacked in the log-scale, since they have
 158 similar shape and amplitude (Ross and Ben-Zion, 2016). The final spectral ratio is obtained by
 159 dividing the target spectrum with the stacked EGF spectrum.

160 To estimate source parameters from spectral ratio, we first fit the omega-square source
 161 model proposed by Boatwright (1980) for the estimation of corner frequency:

$$162 \quad \frac{u_1(f)}{u_2(f)} = \frac{M_{01}}{M_{02}} \sqrt{\frac{1 + \left(\frac{f}{f_{c2}}\right)^4}{1 + \left(\frac{f}{f_{c1}}\right)^4}}, \quad (1)$$

163 where sub-index 1 and 2 represent the target event and EGF, respectively; u is the spectrum, M_0
 164 is the seismic moment, f_c is the corner frequency. Grid search of the moment ratio M_{01}/M_{02} and
 165 two corner frequency f_{c1} and f_{c2} is applied to fit the spectral ratio. In this process, the summed
 166 difference between predicted and observed spectral ratio on a frequency band of 0.2-20Hz is
 167 minimized in the logarithm scale. The source radius is estimated according to Madariaga (1976)'s
 168 theory, assuming a constant rupture velocity of $0.9v_s$:

$$169 \quad r = \frac{0.21v_s}{f_c}, \quad (2)$$

170 where v_s is the S wave velocity, which is set as 3.4-km/s, based on the local velocity structure (Liu
 171 et al., 2021). The average slip on the circular fault is thus:

$$172 \quad D = \frac{M_0}{\mu\pi r^2}, \quad (3)$$

173 where μ is the shear modulus, and is set to 32 GPa. The static stress drop is estimated by Eshelby
 174 (1957)'s equation:

$$175 \quad \Delta\sigma = \frac{7}{16} \frac{M_0}{r^3}. \quad (4)$$

176
177
178
179
180
181
182
183
184
185
186
187
188
189
190
191
192
193
194
195
196
197
198
199
200
201
202
203

2.3 Multi-Point-Source Moment Tensor Inversion

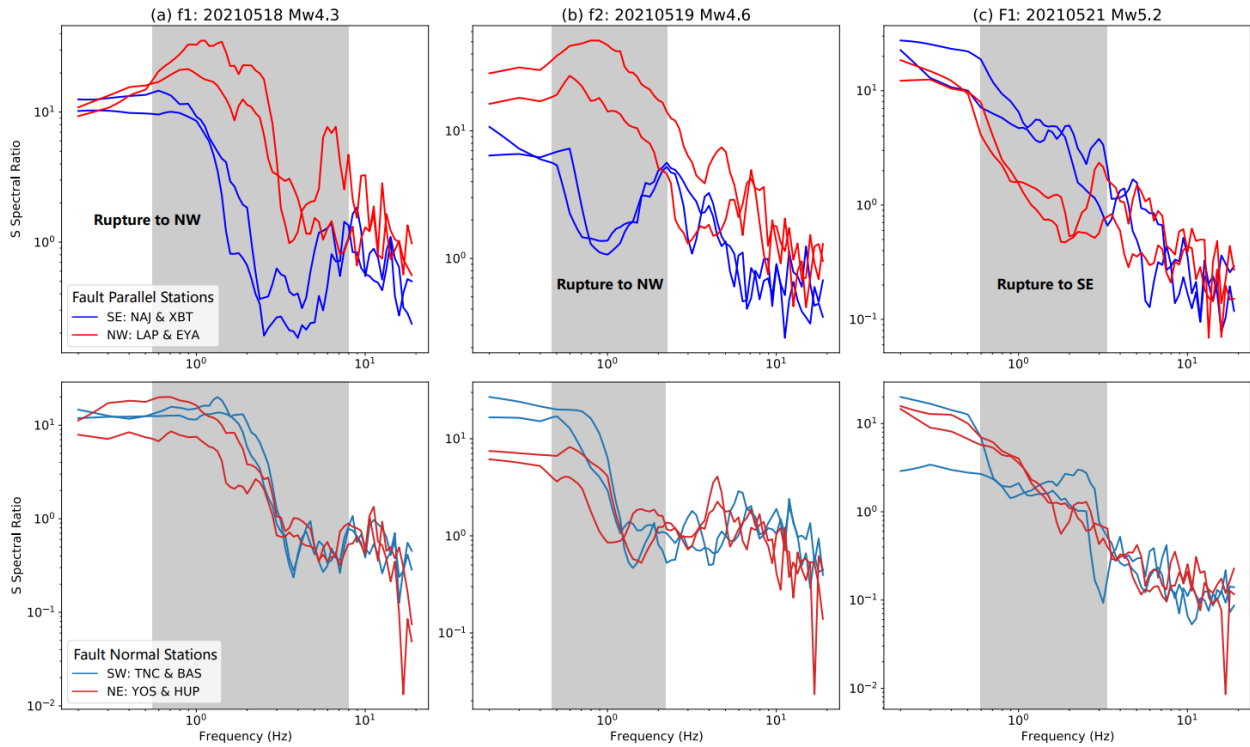
We adopt multi-point-source (MPS) inversion technique (Yue and Lay, 2020) to resolve the moment tensor of the largest foreshock and the mainshock. The MPS method utilize different subevents to model three-component broad-band records in the near field. It is primarily developed by (Kikuchi and Kanamori, 1982; 1986; 1991), and is improved by Yue and Lay (2020) with an iterative inversion algorithm. In this method, a priori constraints are set on the search time window of subevents, their potential location (mesh grids), and the shape of STF. The algorithm finally provides an estimation of the location, initiative time, focal mechanism, and moment of each subevent. This method has advantages for the largest foreshock of Yangbi, which is followed by two immediate aftershock that contaminate the tail wave (see Section 3.2). Thus, we want to refine the results obtained by gCAP method (e.g., Lei et al., 2021; Zhang et al., 2021). It is worth mentioning that polarity-based methods are not suitable as well, because of the imperfect station coverage and that most stations record upward polarity for *F1* (Figure S5-7).

To apply the MPS method in Yangbi, we first select 14 stations with epicentral distances between 30-160km for the largest foreshock, and 12 stations between 40-200km for the mainshock (Figure S9), considering the clipping effect of the nearest stations. All original waveforms are preprocessed by removing the instrumental response, band-pass filtering to 0.01-0.5Hz, and down-sampling to 10-Hz. Event waveforms are cut from 10-s before the initial P arrivals and ending with 130-s and 100-s time windows for foreshock and mainshock separately. For the computation of Green's function, we adopt the regional velocity model developed by joint-inversion of body and surface wave (Liu et al., 2021). The Green's function is computed with wavenumber-frequency integration algorithm (Zhu and Rivera, 2002) for each preset spatial grid. The spatial grids are distributed in a potential rupture area of about 15*6-km. For the largest foreshock and the mainshock, we respectively sliced 10*6 grids and 10*5 grids (Figure S10), considering the distribution of aftershocks. The selection of search time windows, i.e. window length and number of subevents, is based on the visual inspection on waveform and the inversion process (Text S1). For the largest foreshock, we used two subevents that occur between 0-5s and 5-10s; for the mainshock, we use three subevents during 0-3s, 5-8s, and 8-15s.

204 **3. Results and Discussion**

205 **3.1 Rupture Directivity and Source Parameters of the Major Foreshocks**

206 We first investigate the rupture directivity of the major foreshocks, since it is debatable in
207 some published results (Lei et al., 2021; Zhang et al., 2021), and is essential in the determination
208 of rupture area. As demonstrated in Section 2.2, we use the spectral ratio observed on different
209 stations to determine the directivity. Based on the aftershock distribution and local fault traces
210 (Figure 1b), we consider the major fault trend (SE-NW) as the possible rupture direction. Thus,
211 we made two sets of comparisons along fault-normal and fault-parallel direction (Figure 2, and
212 Figure S1a for adopted stations). It is obvious that the fault-parallel spectral ratios show more
213 significant contrast, indicating that the rupture mainly occurs along the major fault trend, and that
214 $f1$ & $f2$ rupture to the NW direction, while $F1$ rupture to SE. This conclusion agrees with the
215 relative location between the epicenter and aftershocks, but disagrees with Lei et al. (2021) that
216 obtained a NE rupture for $F1$ event, based on waveform fitting assuming different nodal planes.
217 However, their waveform inversion utilized a 70-s time window for S wave, which is biased by
218 two immediate large aftershocks (see next section), and there are no mapped NE-trending
219 conjugate faults associated with $F1$, nor do its aftershocks distribute along that direction. Thus,
220 our spectral ratio analysis determines that the Yangbi sequence is associated with faults that strike
221 in NW-SE direction.



222

223

224

225

226

227

Figure 2. Spectral ratio comparison for directivity determination. (a), (b), and (c) plot the spectral ratio comparison of the foreshock $f1$, $f2$, and $F1$, respectively. The first and second line show the comparison along fault-parallel and fault-normal direction. Each line represents a spectral ratio observation on one station, with the color mark its azimuthal quadrant. The frequency bands with significant contrasts are highlighted by gray patches.

228

229

230

231

232

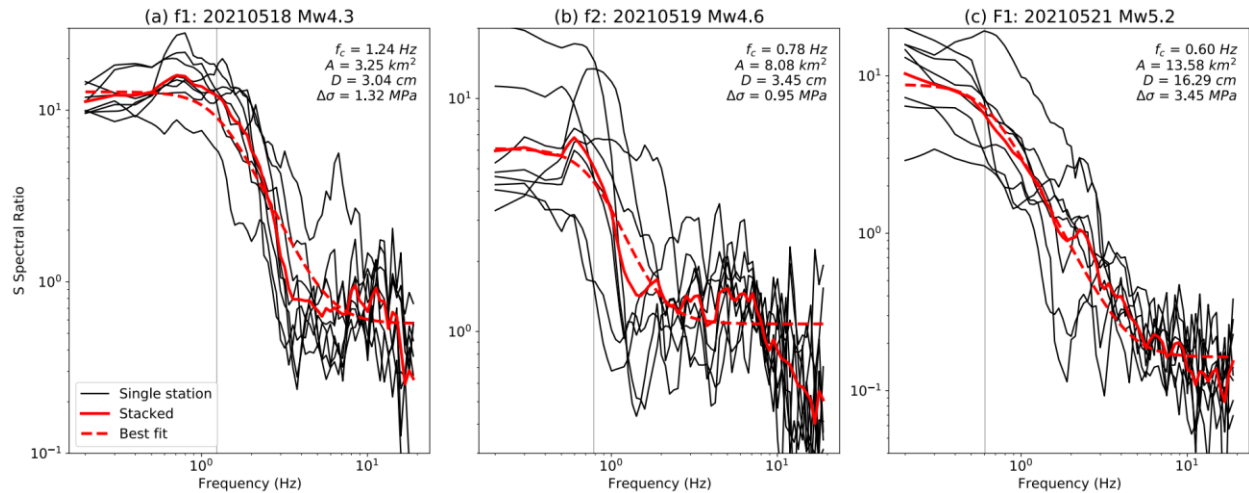
233

234

235

236

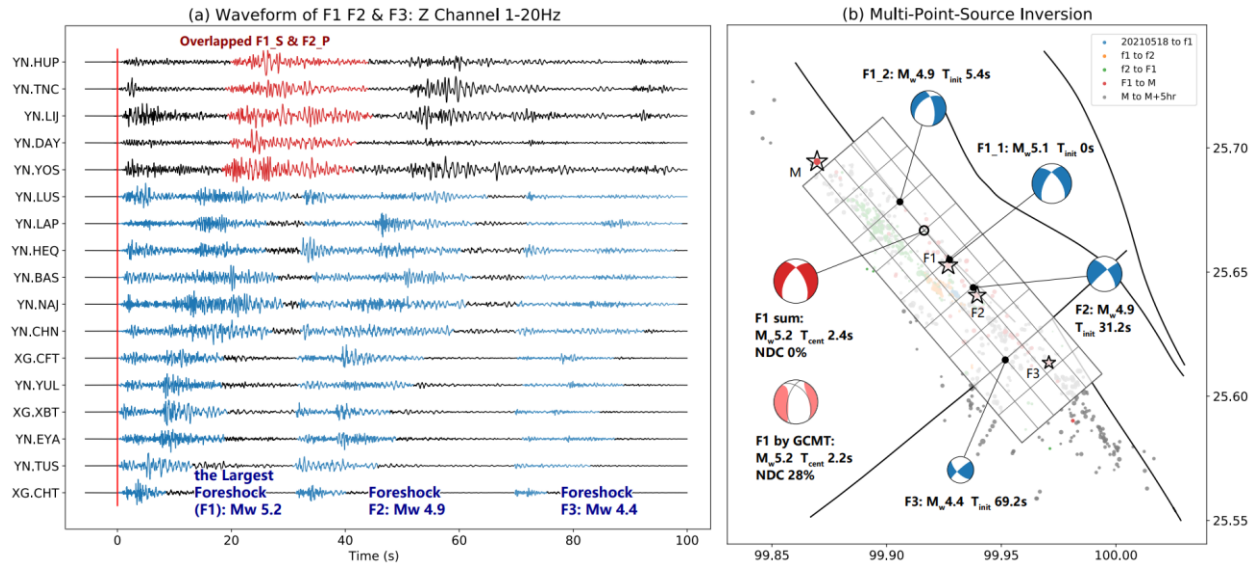
We then extract source parameters for these major foreshocks with fault-normal stations (Figure S1b), where directivity effect is minimized. The spectral ratios on different stations have consistent shape, and the resulting stacked spectral ratio is smooth, fitting well with the Boatwright model (Figure 3). The spectra fitting gives an estimation of corner frequency, which is directly related to the rupture area, assuming Madariaga (1976)'s dynamic model (Equ. 2): for $f1$, $f2$ and $F1$, we got 3.25-km², 8.08-km², and 13.58-km², respectively. The amount of slip and stress drop are also estimated by combining the moment magnitude. We find that $f1$ & $f2$ have relatively low stress drop of ~1.0-MPa and a coseismic slip of 3-cm, while $F1$ has ~3.5-MPa stress drop and ~16-cm coseismic slip (Figure 3).



237
 238 **Figure 3.** Spectral ratio analysis. (a), (b), and (c) plot the spectral ratio analysis of the foreshock $f1$,
 239 $f2$, and $F1$, respectively. The black lines, solid red lines, and dashed red lines denote the spectral ratio on
 240 single stations, stacked spectral ratio, and the best fit to Boatwright model to the stacked spectral ratio. The
 241 vertical gray line marks the estimated corner frequency.

242 **3.2 Analysis of the Largest Foreshock**

243 By inspecting the waveform of $F1$, we found that this largest foreshock of Yangbi is
 244 followed by two immediate aftershocks: M_w 4.9 $F2$ and M_w 4.4 $F3$ (Figure 4a). This raises
 245 challenges in the moment inversion process, since the waveform of different events are overlapped.
 246 Thus, as demonstrated in Section 2.3, we apply MPS inversion technique to $F1-3$, which is
 247 designed to resolve complex rupture process, and is not affected by overlapping waveforms.
 248 Results show that the largest foreshock $F1$ is composed of two subevents (Figure 4b, Text S1),
 249 where the second and smaller subevent $F1_2$ initiates after ~ 5 -s, with its centroid locates at the
 250 NW of the first one. The temporal separation is significantly larger than the duration of an $M \sim 5$
 251 earthquake, which probably indicates that $F1_1$ and $F1_2$ are two independent events that both
 252 rupture to SE. The summarized moment tensor of $F1$ shows a $\sim 60^\circ$ NE dipping nodal plane and
 253 certain normal faulting component. This result is consistent with GCMT result, though our result
 254 show neglectable non-double-couple (NDC) component (Figure 4b). It is not surprising, since
 255 GCMT inverse long-window tele-seismic waveforms that represents an overall moment tensor
 256 including all three events, and that our MPS results show different dip angles between $F1-3$, which
 257 indicates geometrical complexity that can cause NDC in the summarized moment tensor (Julian et
 258 al., 1998).



259

260

261

262

263

264

265

266

Figure 4. Multi-point-source (MPS) inversion for the largest foreshock ($F1$) and its two immediate aftershocks ($F2$ & $F3$). (a) Waveform of $F1$, $F2$, and $F3$. The Z-channel waveform is band-pass filtered to 1-20Hz. The earthquake signal of $F1-3$ are highlighted in blue. The relative remote stations with the S wave of $F1$ and P wave of $F2$ overlapped are marked in red. (b) The MPS inversion result of $F1-3$. The subevents of the whole sequence are marked in blue, with their centroid location distributed on the preset mesh grids. Note that $F1$ is separated by two subevents, and the summarized moment tensor plot in red, with a comparison with that by GCMT plot in light-red.

267

268

269

270

271

272

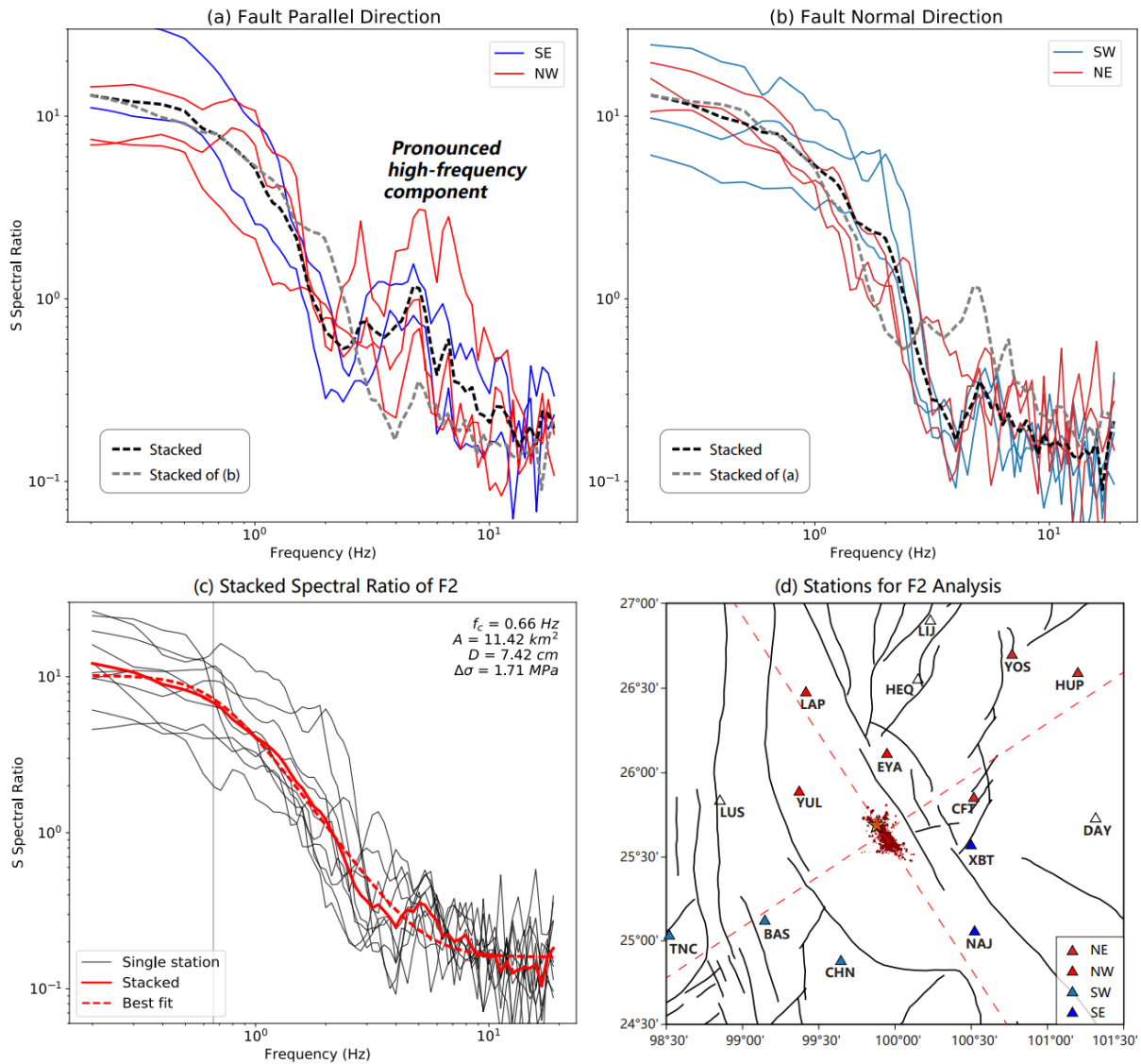
273

274

275

276

The first immediate aftershock, i.e. $F2$, has a similarly large magnitude, thus may play an important role in triggering the mainshock, while is ignored by published results. We apply the spectral ratio analysis demonstrated in Section 2.2 to resolve its rupture source parameters. Note that the spectrum analysis is done with S-wave, which is less biased by the waveform of $F1$. We first examine the rupture directivity. The two-direction comparisons both show weak contrast in corner frequency, indicating bilateral rupturing (Figure 5a, b). However, the fault parallel stations observed pronounced high-frequency component (Figure 5a), suggesting that $F2$ also rupture along the major fault trend. Thus, we adopt the fault-normal stations to extract its source parameters, as in the last section. We obtain a similarly large rupture area ($\sim 11 \text{ km}^2$), but a much smaller coseismic slip ($\sim 7 \text{ cm}$) and stress drop ($\sim 1.7 \text{ MPa}$).

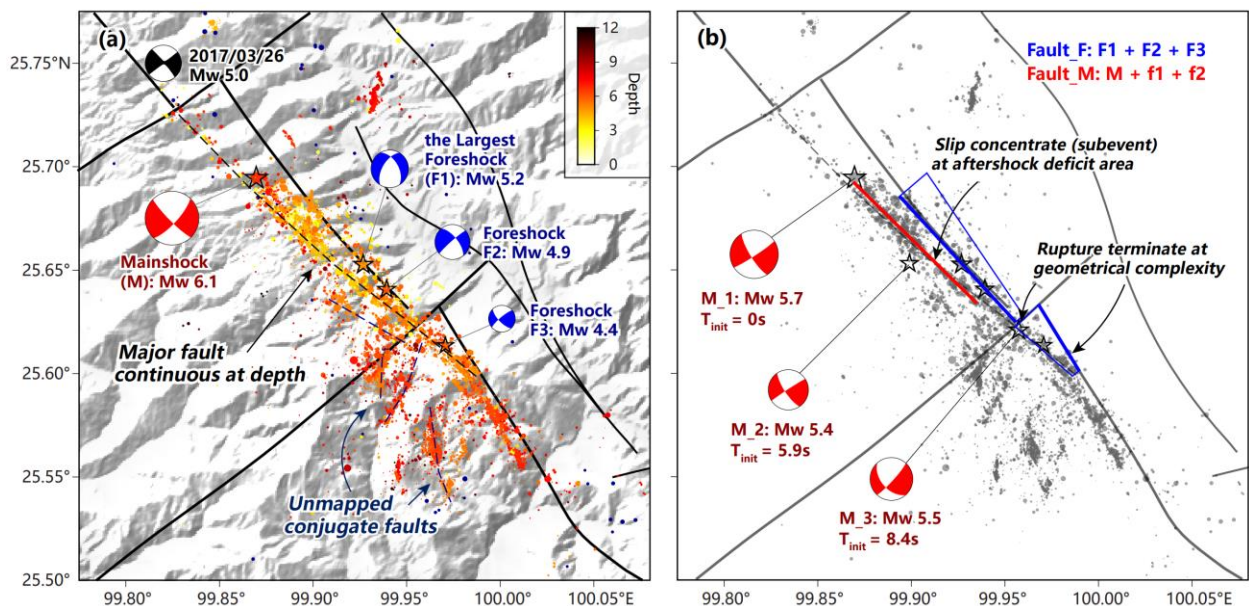


277
 278 **Figure 5.** Spectral ratio analysis of $F2$. (a) & (b) are two sets of spectral ratio comparisons along
 279 fault-parallel and fault-normal direction, respectively. The dash lines are the stacked and averaged spectral
 280 ratio. (c) plots the stacked and fitted spectral ratio. The markers have the same meaning as in Figure 3. (d)
 281 shows the station distribution used in this analysis. Seismic stations are plotted in triangles, fault traces are
 282 plotted in black lines, and reference fault-parallel and fault-normal trend are marked by red dashed lines.

283 3.3 Construction of Fault Model

284 To prepare for the Coulomb stress calculation, we construct a fault model that delineates
 285 the local fault structure and rupture area of each major foreshock. The fault geometry is determined
 286 by the aftershock distribution, focal mechanism, and the mapped local fault traces. The local fault
 287 data show a clear left-lateral step-over feature (Figure 6a), and that the Yangbi mainshock and first

288 two smaller major foreshocks ($f1$ & $f2$) are located off the mapped trace. However, the aftershocks
 289 on the NW of epicenter show a clear trend that connects to another mapped fault segment,
 290 indicating that the major fault is continuous at depth (Figure 6a). This fault segment associated
 291 with M , $f1$, and $f2$ (denoted as $Fault_M$) is probably near-vertical, suggested by their focal
 292 mechanisms (Figure 1b, 6). The largest foreshock $F1$ and its aftershocks are not on $Fault_M$, and
 293 are more likely to occur on the mapped segment (denoted as $Fault_F$), which is dipping to NE, as
 294 indicated by the focal mechanism (Figure 4b, 6a), the relative location between surface fault trace
 295 and microseismic events at depth (Figure 6a), and the aftershock distribution (cross-section CC'
 296 in Figure 7c). The dip angle of $Fault_F$ is likely variable along strike, because the dip angle in the
 297 focal mechanisms of $F1$ & $F2$ are different, and that the aftershock trace is gradually merging with
 298 the surface fault trace (Figure 6). The two fault segments ($Fault_M$ & $Fault_F$) intersect at the
 299 mapped stepover, where multiple unmapped conjugate faults are imaged by aftershocks, indicating
 300 geometrical complexity. This fault segment probably continues to SE at depth, while the surface
 301 trace alters to the mapped stepover, which is supported by the focal mechanism of $F3$ and the third
 302 subevent of M that dip to SW (Figure 6). Though a connected fault makes rupture easier to
 303 propagate, the geometrical complexity causes the termination of mainshock rupture, as shown in
 304 our MPS inversion (Figure 6b) and other studies utilizing joint inversion of InSAR & GPS data
 305 (Li et al., 2022) or InSAR & seismic data (Wang et al., 2022).



307 **Figure 6.** Fault geometry interpretation and MPS inversion of the mainshock. (a) Interpretation of
308 fault geometry. The solid black lines are the mapped fault, the dashed black line is the unmapped major
309 fault, and the dashed dark-blue lines are the unmapped conjugate faults. The blue beachballs mark the MPS-
310 inverted focal mechanisms of the foreshock *F1-3*, and the hollow black stars mark their epicenters. (b)
311 Simplified fault geometry and MPS inversion result of the mainshock. The solid red and blue line marks
312 the simplified fault trace associated with the mainshock and the largest foreshock. The red beachballs mark
313 the focal mechanisms of the mainshock subevents, and their centroid locations are marked by hollow stars.

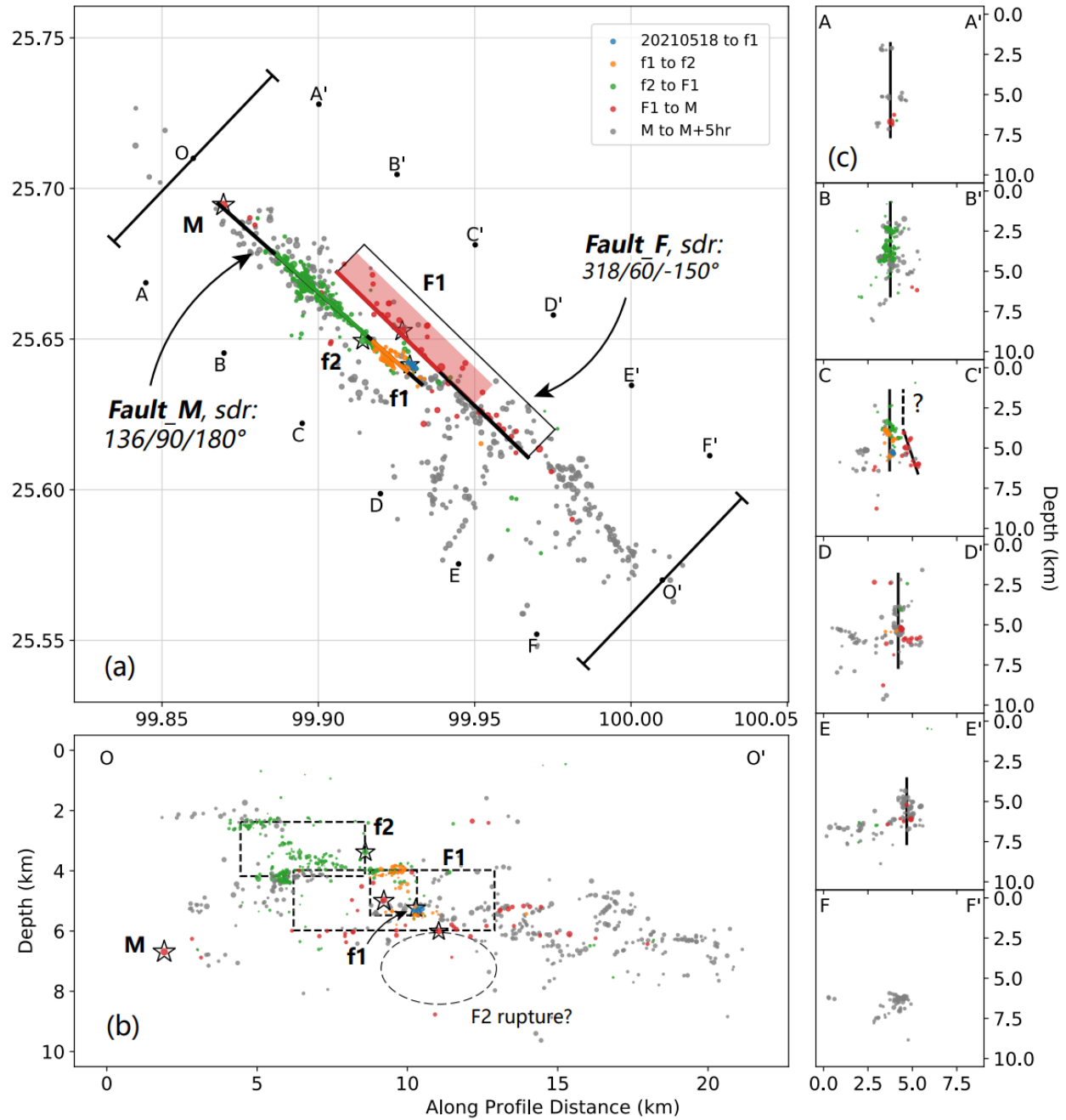
314 The co-seismic rupture of major foreshocks is constrained jointly by aftershock distribution
315 and spectrum-determined rupture area. As demonstrated in the last paragraph, the first two major
316 foreshocks *f1* & *f2* occur on *Fault_M*, which is a near-vertical fault with pure right-lateral strike-
317 slip events initiate on it. Their rupture area is well depicted by the aftershock distribution, because
318 most of the aftershocks occur on only one side of the epicenter (Figure 7a), and that the extension
319 of immediate aftershocks is rather clear (see Section 3.5). We draw a rectangular rupture area of
320 *f1* & *f2* based on their immediate aftershocks (Figure 7a, b), which reach great consistency with
321 the rupture area estimated with spectrum analysis in Section 3.1 (Figure 3a, b).

322 For the largest foreshock *F1*, we first simplify the *Fault_F* as a 60° NE dipping fault that
323 slips with a rake angle of -150° (right-lateral + normal faulting), based on the focal mechanism
324 solution. However, the coseismic rupture cannot be directly imaged from aftershocks, because the
325 immediate aftershocks occur on both sides of the epicenter (though mainly on the SE side), and
326 the total associated rectangular area is significantly larger than that inferred from spectral ratio
327 method. Therefore, we adopt two end-member rupture models for *F1*, and show that this difference
328 does not alter the interpretation of triggering relation (see Section 3.5), while only the preferred
329 model and related Coulomb stress calculation is shown in the main text. The preferred model put
330 the NW end of *F1* rupture on the location of the northernmost immediate aftershock, since the
331 second subevent of *F1* locates on the NW of epicenter (Figure 4b). The southern end of *F1* rupture
332 is set at the fault junction between the major fault and mapped conjugate fault (Figure 6a), which
333 is also near the termination of the mainshock (*M_3*, Figure 6b). The top of *F1* rupture is set at 4-
334 km, since the shallowest aftershock locates at 4-km, and that the shallower portion of the fault is
335 probably near-vertical, so that the fault trace is separated at surface by the observed distance (see
336 cross-section CC' in Figure 7c). This preferred model leads to a rupture area consistent with the
337 spectral ratio analysis (Figure 3c), and the overall rupture directivity is to SE, as shown in Figure

338 2c. Further evidence in support or against this model may come from source-time function
339 extraction and subsequent subevent location technique with a rather dense seismic network (e.g.,
340 López-Comino and Cesca, 2018; Wu et al., 2019; Meng and Fan, 2021).

341 Another important event is the M_w 4.9 $F2$, i.e. the first and largest immediate aftershock of
342 $F1$. As shown by spectrum analysis (see Section 3.2), $F2$ is a bilateral rupture along $Fault_F$ that
343 has a similarly large rupture area as $F1$. Its rupture area is even harder to determine than $F1$, since
344 we cannot decipher which aftershock is associated with $F2$. The best guess we can make is that $F2$
345 ruptures a deeper portion (Figure 7b), which avoids an immediate re-rupturing of the same asperity.
346 Again, further investigations would require near-source stations that can resolve the down-dip
347 rupturing behavior. Based on the above reasons, we decide not to include $F2$ in the Coulomb stress
348 modeling, but will include it in our discussion in Section 3.5.

349 Our fault model of foreshocks forms a complementary pattern with the co-seismic rupture
350 of the M_w 6.1 mainshock that concentrates at about 3-10km initially and propagates towards the
351 shallower portion at SE side at about 2-6km (Li et al., 2022; Wang et al., 2022). This is a typical
352 pattern for aftershock distribution and coseismic slip, as shown in many other case studies (e.g.,
353 Yue et al., 2017; Mendoza et al., 2019; Meng et al., 2021). Based on this model, we can calculate
354 the static Coulomb stress change induced by each foreshock.



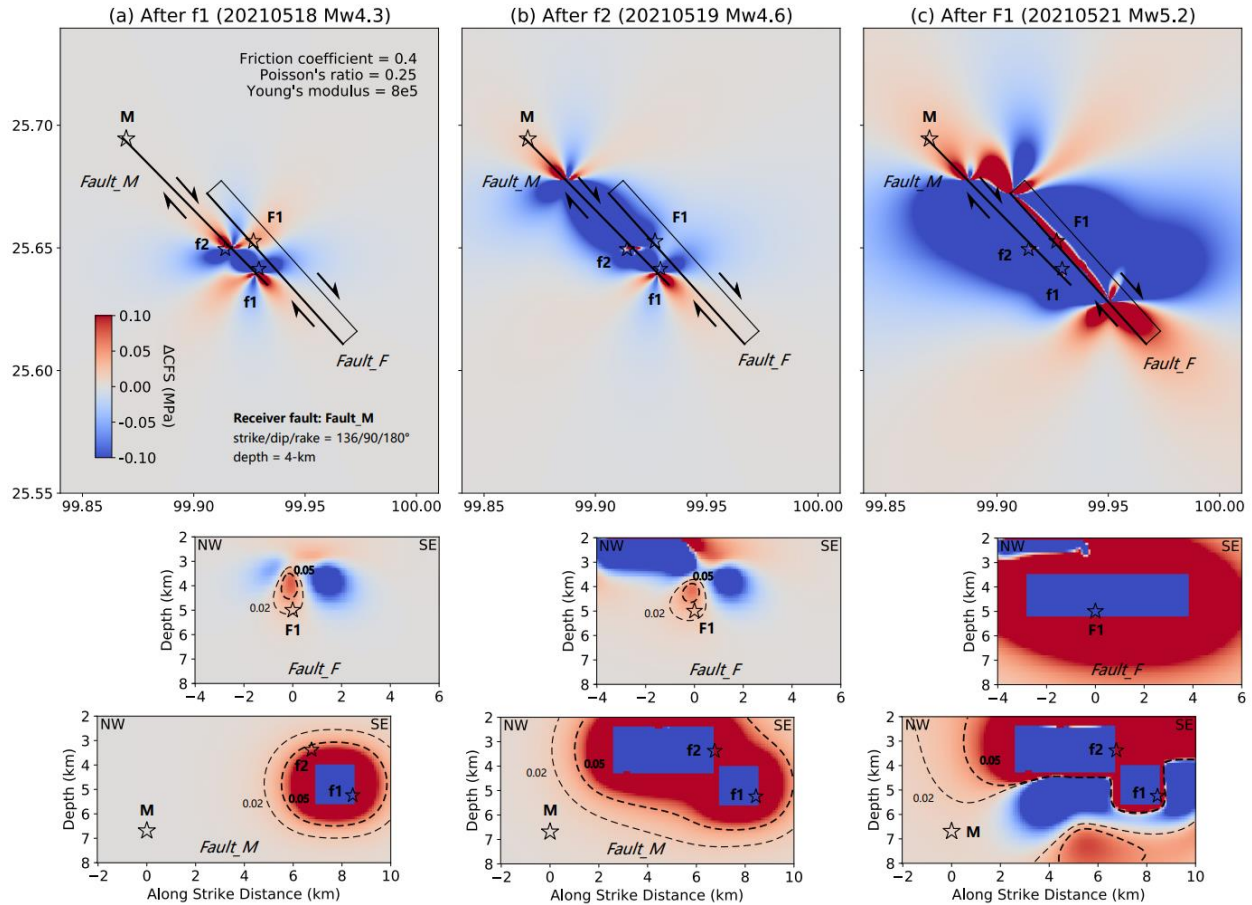
355
 356
 357
 358
 359
 360

Figure 7. Distribution of seismic events and finite rupture model. (a) Map view, (b) cross-section along strike, and (c) fault-normal cross-sections. Events in different periods are denoted by colors. Four major foreshocks are marked by hollow stars. The simplified faults associated with the mainshock (*Fault_M*) and the largest foreshock (*Fault_F*) are denoted as thick black lines. The rupture length and area are marked by color line and patch in (a) and dashed black rectangles in (b).

361 **3.4 Coulomb Stress Evolution**

362 We calculate the static change of Coulomb failure stress (ΔCFS) with the Coulomb 3
363 software (Lin and Stein, 2004; Toda et al., 2005), which assumes a homogeneous elastic half-space.
364 The fault patch and amount of slip are determined according to the previous section. The friction
365 parameters are set as default: Coefficient of friction = 0.4, Poisson's ratio = 0.25, Young's modulus
366 = 8×10^4 MPa. We calculated the cumulated Coulomb stress change after each significant foreshock
367 (Figure 8).

368 Results show that the foreshock $f1$ causes a significant increase of ΔCFS near the
369 hypocenter of $f2$ (Figure 8a), indicating a cascade triggering. Note that $f1$ also promotes the
370 occurrence of $F1$, with a $\Delta CFS \approx 0.02 \text{ MPa}$. Similarly, the foreshock $f2$ causes positive ΔCFS on
371 both $F1$ and M as well (Figure 8b). For $F1$, the net effect of $f1$ & $f2$ caused a $\Delta CFS > 0.02 \text{ MPa}$,
372 which, though small, is above the traditionally considered threshold of 0.01-MPa for static
373 triggering (e.g., Hardebeck et al., 1998; Ziv and Rubin, 2000; Parsons and Velasco, 2009). Note
374 that the positive effect of $f2$ on $Fault_F$ rupturing is localized within 1-2km, which covers the
375 separation of these two faults (Figure S17). The occurrence of $F1$ pushes the 0.02-MPa ΔCFS
376 boundary closer to the hypocenter of M , which is also true for another rupture model of $F1$ that is
377 purely unilateral towards SE (Figure S15-16). Again, this number is not significantly large
378 compared with many statistical studies (e.g., King et al., 1994; Kilb et al., 2002), but is considered
379 sufficient to explain the triggering in many other studies (Steady et al., 2005, and references
380 therein). More detailed discussions on the causality are presented in the next section.



381
 382 **Figure 8.** Evolution of Coulomb stress change. (a), (b), and (c) plot cumulated Coulomb stress
 383 change after $f1$, after $f2$, and after $F1$, respectively. The hypocenters are marked by stars. The upper and
 384 lower panels plot the map view with $Fault_M$ as the receiver fault, and the cross-sections on $Fault_M$ and
 385 $Fault_F$. Contours of 0.02-MPa and 0.05-MPa Coulomb stress increase are marked by dashed lines.

386 3.5 Interpretation of Inter-Event Triggering

387 3.5.1 How do the M_w 4.3 $f1$ & M_w 4.6 $f2$ initiate?

388 The initiation of $f1$ is preceded by a micro-seismic swarm near the hypocenter (Figure 1b,
 389 7a, 9a), probably indicating the nucleation process (Dieterich, 1992; Ampuero and Rubin, 2008).
 390 Similar highly clustered seismicity before a major earthquake is also observed in the 2019 M_w 6.4
 391 Ridgecrest foreshock (Shelly, 2020) and the 2007 M_w 4.6 Odaesan, Korea, earthquake (Kim et al.,
 392 2010). This observation differs from Zhang et al. (2021) who claims no nucleation signal in Yangbi,
 393 but is consistent with the plots in Liu et al. (2022). It is clear in the fault-parallel profile that the
 394 asperity of $f1$ is isolated from that of $f2$ (Figure 7b, 9c), which explains why $f1$ cannot rupture to a
 395 wider extent. The neighboring location of $f1$ asperity & $f2$ hypocenter and the large Coulomb stress

396 increase (Figure 8a) strongly indicate a cascade triggering mechanism. However, the static
397 triggering theory cannot explain the time delay between events (Freed, 2005; Steacy et al., 2005).
398 The ~20-hr time delay between *f1* and *f2* may be explained by further stress accumulation from
399 afterslip or the nucleation process.

400 **3.5.2 How does the M_w 5.2 *F1* initiate?**

401 As demonstrated in Section 3.4, *f2* itself causes a >0.01-MPa Coulomb stress increase on
402 the NW segment of *Fault_F* (Figure 8b, S17), which is sufficient to declare a static triggering
403 effect. However, *f1* also plays a role in preparing for the initiation of *F1*, and the Coulomb stress
404 increase is localized around the *F1* hypocenter (Figure 8a). Thus, it is probably *f1* that determines
405 the hypocenter of *F1*. Another noticeable feature of the *f2*-induced ΔCFS is that it become negative
406 above ~4-km, which is the lower boundary of *f2* rupture area. This may confine the *F1* hypocenter
407 and its rupture area below 4-km, which is consistent with our setting of the fault model (Figure 7b,
408 9c). At the hypocentral depth of *F1* (~5-km), the positive effect of *f2* is more significant on the
409 NW portion of *Fault_F* (Figure S17, 8b), which favors a second subevent on NW (as in Figure
410 4b), and that the rupture of *F1* is more likely has an extension to NW, instead of a purely SE-
411 propagating unilateral rupture, as argued in Section 3.3.

412 While the static Coulomb stress change of *f1* & *f2* is sufficient to explain the occurrence of
413 *F1*, we want to note here that some possible aseismic signals are also captured and may contribute
414 to the triggering process. The aftershock zone of *f2* slightly expands along two sides of the
415 coseismic rupture: ~1-km towards the NW side, and ~2-km to the SE side (Figure 9a). This
416 migration of aftershock is probably driven by afterslip, a widely observed post-seismic relaxation
417 phenomenon (Perfettini and Avouac, 2004; Kato, 2007; Barbot et al., 2009; Peng and Zhao, 2009;
418 Meng and Peng, 2015). Note that the SE-propagating afterslip occurs on the area above *f1*, which
419 would cause a positive Coulomb stress change on *F1*. Again, this mechanism can well explain the
420 time delay between the occurrence of *f2* and *F1*. The possible afterslip towards NW will be
421 discussed in the next subsection. Moreover, like *f1*, the largest foreshock *F1* is also preceded by
422 an increasing occurrence of micro-seismic events near its hypocenter, though in a much shorter
423 period and with much fewer events (Figure 9b). This swarm may imply the existence of pre-slip
424 during nucleation or is a mini mainshock-aftershock sequence triggered by the afterslip of *f2*.

425 **3.5.3 How does the M_w 6.1 M initiate?**

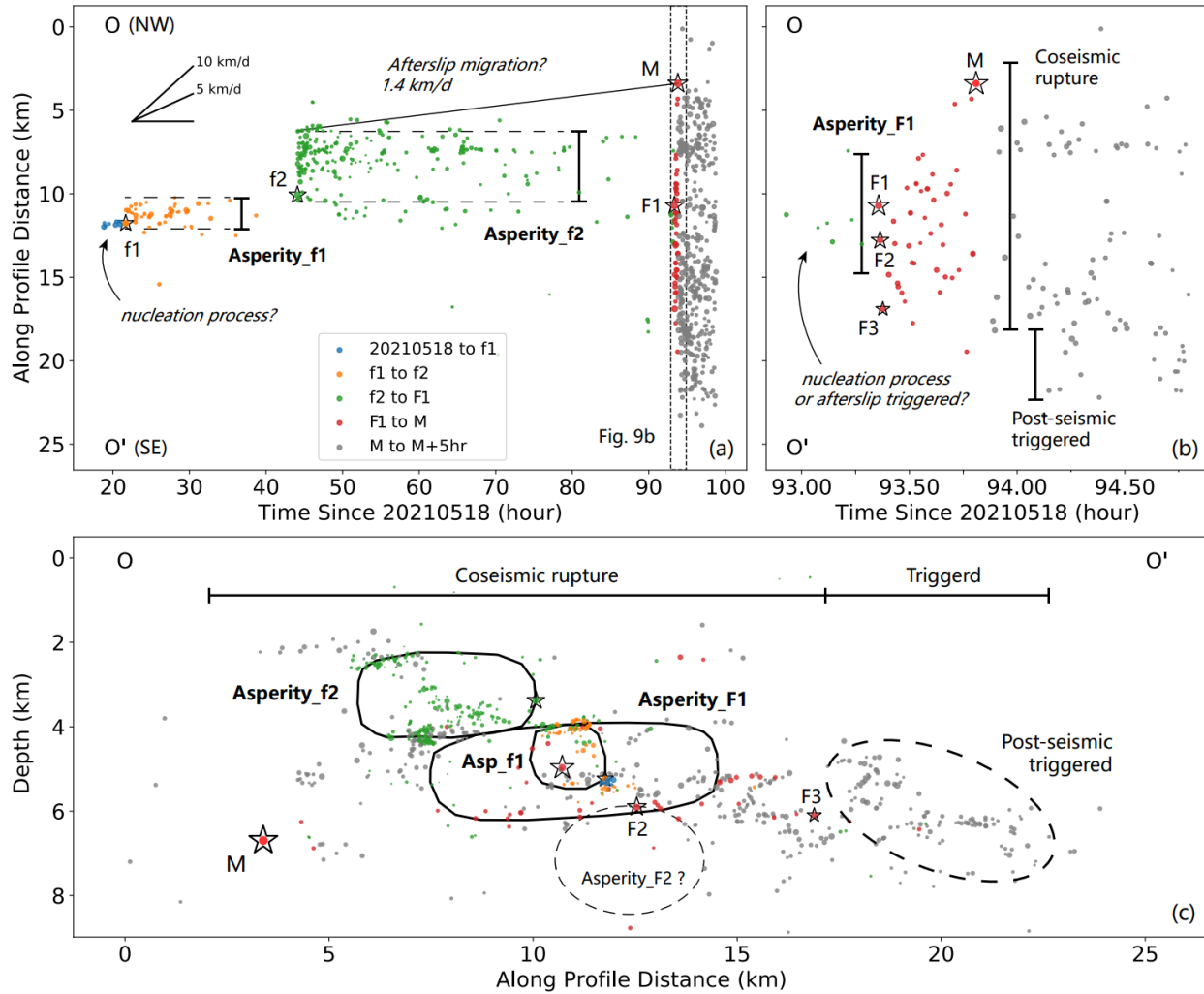
426 Our Coulomb stress modeling shows that both f_2 and $F1$ draw positive but relatively small
427 ΔCFS on the mainshock hypocenter, but their summarized effect reaches a commonly adopted
428 static triggering threshold of 0.01-MPa (Figure 8b, c). However, this may not be a satisfactory
429 interpretation, since the short time interval between $F1$ and M (~30-min) strongly indicates that
430 the mainshock nucleation area has been critically stressed before $F1$ or/and is significantly
431 triggered by/after $F1$. Two other factors are likely incorporated in the triggering process: the
432 afterslip of f_2 and the rupture of $F2$.

433 As pointed out in the last subsection, the aftershock zone of f_2 shows an expansion towards
434 both sides along $Fault_M$, indicating an afterslip migration. The NW migrating afterslip would
435 cause a positive Coulomb stress change on M , driving it closer to failure. Based on the aftershock
436 evolution (Figure 9a), the average migration velocity can be estimated as 1.4-km/d, if we assume
437 that the mainshock is initiated immediately when the creep front reaches its epicenter. It is also
438 possible that the afterslip zone does not completely fill the gap between f_2 rupture and M , since a
439 ~1.5-km gap on the NW is not filled by migrated aftershocks (Figure 9a). However, the magnitude
440 of f_2 is too small (M_w 4.6) to generate visible afterslip for GPS, thus makes it difficult to validate
441 the existence and extension of afterslip. Though no direct evidence in Yangbi, afterslip generated
442 by M 4-5 or even smaller earthquakes have been observed in California with borehole strain data,
443 and they tend to release a higher ratio of coseismic moment compared with that of large
444 earthquakes (Hawthorne et al., 2016; Alwahedi and Hawthorne, 2019). If the $Fault_M$ is already
445 critically stressed before $F1$, it would be susceptible to small static stress change or even dynamic
446 stress of $F1$ (Freed, 2005; Yun et al., 2019).

447 We point out in Section 3.3 that the rupture area of $F2$ is hard to determine, which prevents
448 us from obtaining an accurate ΔCFS modeling. However, $F2$ has a comparable magnitude (M_w 4.9)
449 as the largest foreshock $F1$, and the NW end of its rupture area probably reaches near the $F1$
450 epicenter (Figure 7b, 9c), which suggests a non-negligible triggering effect. Similar to the ΔCFS
451 by pure-unilateral $F1$ rupture model (Figure S16), we suspect that $F2$ could cause a 0.01-0.02MPa
452 Coulomb stress increase, which is comparably large as the contribution from $F1$.

453 Thus, the occurrence of Yangbi mainshock is probably a joint result of multiple major
454 foreshocks that combines both seismic and aseismic process. It becomes the mainshock by chance,
455 because its hypocenter is not the first to nucleate, or those major foreshocks would likely become

456 its aftershock, or part of its rupture process. Such unpredictable feature fit better with the cascade
 457 model demonstrated in the Introduction (Helmstetter et al., 2003; Felzer et al., 2004; Ellsworth
 458 and Bulut, 2018; Yoon et al., 2019).



459
 460 **Figure 9.** Migration pattern and interpretation of triggering mechanism. (a) and (b) plot seismicity
 461 migration along strike. The reference points OO' are the same as in Figure 7. The extension of different
 462 asperities is marked by vertical lines. (c) plot fault-parallel cross-section, with the rough boundary of
 463 asperity delineated by solid lines.

464 3.5.4 Comparison with Published Results

465 As discussed in previous subsections, we find that Yangbi sequence is basically a cascade
 466 sequence, while aseismic signals probably exist and play an important role in the triggering process.

467 However, many published studies reach different conclusions. Here, we provide a brief review and
468 comparisons on those results.

469 Similar as our conclusion, the cascade model is preferred by Zhang et al. (2021) and Liu et
470 al. (2022), both of which point out that the major foreshocks occur in a random behavior, and there
471 is no consistent migration direction. However, Zhang et al. (2021) argues that no aseismic signals
472 can be found, e.g. repeaters, while Liu et al. (2022) argues that *F1* is triggered by aseismic slip
473 based on the fact that *f1* & *f2* cause negative Coulomb stress change. We consider both of the
474 arguments have certain flaw: (1) we do observe some indicators for aseismic slip, e.g. the pre-
475 event cluster in *f1* and the aftershock zone expansion in *f2* (see Section 3.5); (2) the negative ΔCFS
476 resulted in Liu et al. (2022) is caused by an inaccurate event location and rupture model (see
477 Section 3.4).

478 Tidal triggering is proposed by Lei et al. (2021), who reaches this conclusion because the
479 major events coincide with the peak values of tidal strain and tidal shear & normal stress. However,
480 this inference is not rigorous, since (1) the triggering effect should be decided on Coulomb stress,
481 instead of strain, shear, or normal stress, and that those major events initiate at times of near-zero
482 or even negative tidal-induced Coulomb stress change; (2) the tidal effect causes too small stress
483 change, which is 2-orders smaller than coseismic stress transfer. Thus, we disagree that the
484 observations in Lei et al. (2021) can indicate tidal triggering.

485 The tidal sensitive observation given by Lei et al. (2021) lead to another deduction that
486 fluid plays an important role in the Yangbi sequence, which is supported by Sun et al. (2022), who
487 detected an area of high V_P/V_S ratio at about 18-30km beneath the Yangbi sequence. However,
488 both studies show no direct evidence for the existence of fluids and fluid upwelling, and the
489 seismicity pattern in Yangbi is very different from that driven by fluid, e.g. 2009 L'Aquila
490 sequence, where the seismicity migrates along a consistent direction and follows the fluid diffusion
491 law (Di Luccio et al., 2010; Chiaraluce et al., 2011; Cabrera et al., 2022). Further investigations
492 on the existence and effects of fluid may include extracting time-dependent V_P/V_S pattern (e.g., Di
493 Luccio et al., 2010; Lin, 2020), long-term search for fluid-driven seismicity migration, and
494 statistical analysis of source parameters (e.g., stress drop, Cabrera et al., 2022).

495

3.6 Implications on Foreshock Triggering Modes

496

497

498

As reviewed in the Introduction, cascade-up and pre-slip model are two end-member models for foreshock mechanism. However, with accumulating observational studies, the understanding becomes more complicated:

499

500

501

502

503

(1) The inter-event triggering in cascade model can be realized through aseismic slip as well, i.e. the afterslip of large foreshocks. For example, the 2016 M_w 7.0 Kumamoto earthquake is triggered by both the static stress change and the afterslip of M_w 6.2 foreshock (Kato et al., 2016). However, the inclusion of aseismic slip does not help predict the initiation time and size of the mainshock, which is similar as what we observed in Yangbi.

504

505

506

507

508

509

510

511

512

(2) Slow-slip events can be an external driven source that triggers both the foreshock and the mainshock. This kind of triggering mechanism is also widely observed, e.g. the 2011 M_w 9.0 Tohoku (Kato et al., 2012), the 2014 M_w 8.1 Iquique (Kato and Nakagawa, 2014; Ruiz et al., 2014), and the 2017 M_w 6.9 Valparaiso earthquake (Ruiz et al., 2017). Again, the aseismic slip in such mechanism does not provide predictability on the magnitude of mainshock, but the migration direction of foreshock sequence does give a clue of where the mainshock may occur. This mechanism serves as another mode besides cascading and pre-slip model, and thus implies that only searching for aseismic-slip-indicators is not enough in the discrimination of foreshock triggering modes.

513

514

515

516

517

518

519

520

521

(3) For the pre-slip nucleation phase, we still lack direct observations in the field. Near field observations with bore-hole strain meter have reported no similar nucleation signals so far (Roeloffs, 2006), even before the 2004 Parkfield earthquake (Johnston et al., 2006). Meng and Fan (2021) detect immediate foreshocks in the 2019 Ridgecrest aftershocks, but found that they follow mostly the cascade mode, with no scaling between the characteristic of their P wave and the magnitude of target event. Though Tape et al. (2018) reports possible nucleation signals in the strike-slip fault system in central Alaska, it comes in the form of very-low-frequency earthquakes, instead of significant foreshocks. It may be interesting to perform large-scale statistics on the candidate pre-slip clusters like that preceding *f1* in our study.

522

523

524

525

(4) Multiple mechanisms can coexist in a foreshock-mainshock sequence. Based on recent laboratory observations, McLaskey (2019) proposes a rate-dependent cascade-up model that includes contributions from both cascade-up and pre-slip mechanism. Case studies have also indicated such dual-mode mechanism in foreshock sequences, e.g. the 2009 M_w 6.3 L'Aquila

526 earthquake (Cabrera et al., 2022), the 2010 M_w 7.2 El-Mayor earthquake (Yao et al., 2020), and
527 the 2019 M_w 7.1 Ridgecrest earthquake (Huang et al., 2020; Yue et al., 2021).

528 **4. Conclusions**

529 In this paper, we utilize seismological methods to characterize the 2021 Yangbi foreshock
530 sequence, in the purpose of analyzing the causality between the major events. We find that the
531 Yangbi sequence is associated with a rather complex fault geometry, with the mainshock and two
532 smaller foreshocks occur on an unmapped near-vertical fault, and the largest foreshock occurs on
533 a mapped stepover fault that dips to NE. The geometrical complexity confines the rupture
534 extension of the mainshock and some foreshocks. Coulomb stress modeling shows that the
535 foreshock triggering process can be explained by cascade triggering, while we also find evidence
536 for aseismic slip that contributes to the triggering process. We conclude that the nucleation of
537 mainshock is the result of multiple major foreshocks with both seismic and aseismic process, and
538 that the formation of this foreshock-mainshock sequence is probably a coincidence. This detailed
539 observation lend supports to the developed understanding on foreshock triggering mechanism: (1)
540 the foreshock model is not limited to cascade-up & pre-slip, multiple mechanisms can operate
541 together; and (2) aseismic slip does not always provide more predictability on the mainshock.

542 **Acknowledgments**

543 We thank the Yunnan Earthquake Agency for providing the continuous seismic data; Prof.
544 Zhonghai Wu for sharing the local fault trace data; Dr. Baoning Wu, Prof. Zhigang Peng, and Prof.
545 Daoyuan Sun for valuable suggestions in preparing the paper. Figures in this paper are plotted with
546 Matplotlib and GMT. The python implementation of multi-taper method (Prieto et al., 2009) is
547 available at <https://github.com/krischer/mtspeg>. The Coulomb-3 software is available at
548 <https://www.usgs.gov/node/279387>. This research is supported jointly by the National Key R&D
549 Program of China (2021YFC3000702), the Nature Science Foundation of China projects (grants
550 no. U2139205 & U2039204), US National Science Foundation (award number 1941719).

551 **Data Availability**

552 Seismic catalog used in this paper is available on Github:

553 <https://doi.org/10.5281/zenodo.5548377> ([https://github.com/YijianZhou/Seismic-](https://github.com/YijianZhou/Seismic-Catalog/blob/main/zhou_eqs-2021_Yangbi_pal-cerp-mess.ctlg)
554 [Catalog/blob/main/zhou_eqs-2021_Yangbi_pal-cerp-mess.ctlg](https://github.com/YijianZhou/Seismic-Catalog/blob/main/zhou_eqs-2021_Yangbi_pal-cerp-mess.ctlg)).

555

556 References

- 557 Alwahedi, M. A., and J. C. Hawthorne (2019). Intermediate-Magnitude Postseismic Slip Follows
558 Intermediate-Magnitude (M 4 to 5) Earthquakes in California, *Geophysical Research*
559 *Letters*, 46(7), 3676-3687, doi:<https://doi.org/10.1029/2018GL081001>.
- 560 Ampuero, J.-P., and A. M. Rubin (2008). Earthquake nucleation on rate and state faults – Aging
561 and slip laws, *Journal of Geophysical Research: Solid Earth*, 113(B1),
562 doi:<https://doi.org/10.1029/2007JB005082>.
- 563 Barbot, S., Y. Fialko, and Y. Bock (2009). Postseismic deformation due to the Mw 6.0 2004
564 Parkfield earthquake: Stress-driven creep on a fault with spatially variable rate-and-state
565 friction parameters, *Journal of Geophysical Research: Solid Earth*, 114(B7),
566 doi:<https://doi.org/10.1029/2008JB005748>.
- 567 Boatwright, J. (1980). A spectral theory for circular seismic sources; simple estimates of source
568 dimension, dynamic stress drop, and radiated seismic energy, *Bulletin of the Seismological*
569 *Society of America*, 70(1), 1-27, doi:10.1785/bssa0700010001.
- 570 Bouchon, M., H. Karabulut, M. Aktar, S. Özalaybey, J. Schmittbuhl, and M.-P. Bouin (2011).
571 Extended Nucleation of the 1999 Mw7.6 Izmit Earthquake, *Science*, 331(6019), 877-880,
572 doi:10.1126/science.1197341.
- 573 Cabrera, L., P. Poli, and W. B. Frank (2022). Tracking the Spatio-Temporal Evolution of
574 Foreshocks Preceding the Mw 6.1 2009 L'Aquila Earthquake, *Journal of Geophysical*
575 *Research: Solid Earth*, 127(3), e2021JB023888,
576 doi:<https://doi.org/10.1029/2021JB023888>.
- 577 Calderoni, G., A. Rovelli, Y. Ben-Zion, and R. Di Giovambattista (2015). Along-strike rupture
578 directivity of earthquakes of the 2009 L'Aquila, central Italy, seismic sequence,
579 *Geophysical Journal International*, 203(1), 399-415, doi:10.1093/gji/ggv275.
- 580 Calderoni, G., A. Rovelli, and R. Di Giovambattista (2017). Rupture Directivity of the Strongest
581 2016–2017 Central Italy Earthquakes, *Journal of Geophysical Research: Solid Earth*,
582 122(11), 9118-9131, doi:<https://doi.org/10.1002/2017JB014118>.
- 583 Chen, X., and P. M. Shearer (2013). California foreshock sequences suggest aseismic triggering
584 process, *Geophysical Research Letters*, 40(11), 2602-2607,
585 doi:<https://doi.org/10.1002/grl.50444>.
- 586 Chiaraluce, L., L. Valoroso, D. Piccinini, R. Di Stefano, and P. De Gori (2011). The anatomy of
587 the 2009 L'Aquila normal fault system (central Italy) imaged by high resolution foreshock
588 and aftershock locations, *Journal of Geophysical Research: Solid Earth*, 116(B12),
589 doi:<https://doi.org/10.1029/2011JB008352>.
- 590 Di Luccio, F., G. Ventura, R. Di Giovambattista, A. Piscini, and F. R. Cinti (2010). Normal faults
591 and thrusts reactivated by deep fluids: The 6 April 2009 Mw 6.3 L'Aquila earthquake,
592 central Italy, *Journal of Geophysical Research: Solid Earth*, 115(B6),
593 doi:<https://doi.org/10.1029/2009JB007190>.
- 594 Dieterich, J. H. (1978). Preseismic fault slip and earthquake prediction, *Journal of Geophysical*
595 *Research: Solid Earth*, 83(B8), 3940-3948, doi:<https://doi.org/10.1029/JB083iB08p03940>.
- 596
- 597 Dieterich, J. H. (1992). Earthquake nucleation on faults with rate-and state-dependent strength,
598 *Tectonophysics*, 211(1), 115-134, doi:[https://doi.org/10.1016/0040-1951\(92\)90055-B](https://doi.org/10.1016/0040-1951(92)90055-B).
- 599 Dodge, D. A., G. C. Beroza, and W. L. Ellsworth (1996). Detailed observations of California
600 foreshock sequences: Implications for the earthquake initiation process, *Journal of*

601 *Geophysical Research: Solid Earth*, 101(B10), 22371-22392,
602 doi:<https://doi.org/10.1029/96JB02269>.

603 Ellsworth, W. L., and F. Bulut (2018). Nucleation of the 1999 Izmit earthquake by a triggered
604 cascade of foreshocks, *Nature Geoscience*, 11(7), 531-535, doi:10.1038/s41561-018-0145-
605 1.

606 Eshelby, J. D. (1957). The determination of the elastic field of an ellipsoidal inclusion, and related
607 problems, *Proceedings of the Royal Society of London. Series A. Mathematical and*
608 *Physical Sciences*, 241(1226), 376-396, doi:10.1098/rspa.1957.0133.

609 Felzer, K. R., R. E. Abercrombie, and G. r. Ekström (2004). A Common Origin for Aftershocks,
610 Foreshocks, and Multiplets, *Bulletin of the Seismological Society of America*, 94(1), 88-98,
611 doi:10.1785/0120030069.

612 Freed, A. M. (2005). Earthquake Triggering by Static, Dynamic, and Postseismic Stress Transfer,
613 *Annual Review of Earth and Planetary Sciences*, 33(1), 335-367,
614 doi:10.1146/annurev.earth.33.092203.122505.

615 Han, Z.-j., S.-m. Guo, H.-f. Xiang, J.-s. Zhang, and Y.-k. Ran (2004). Seismotectonic environment
616 of occurring the February 3, 1996 Lijiang M=7.0 earthquake, Yunnan province, *Acta*
617 *Seismologica Sinica*, 17(4), 453-463, doi:10.1007/s11589-004-0025-1.

618 Hardebeck, J. L., J. J. Nazareth, and E. Hauksson (1998). The static stress change triggering model:
619 Constraints from two southern California aftershock sequences, *Journal of Geophysical*
620 *Research: Solid Earth*, 103(B10), 24427-24437, doi:<https://doi.org/10.1029/98JB00573>.

621 Haskell, N. A. (1964). Total energy and energy spectral density of elastic wave radiation from
622 propagating faults, *Bulletin of the Seismological Society of America*, 54(6A), 1811-1841,
623 doi:10.1785/bssa05406a1811.

624 Hawthorne, J. C., M. Simons, and J.-P. Ampuero (2016). Estimates of aseismic slip associated
625 with small earthquakes near San Juan Bautista, CA, *Journal of Geophysical Research:*
626 *Solid Earth*, 121(11), 8254-8275, doi:<https://doi.org/10.1002/2016JB013120>.

627 Helmstetter, A., D. Sornette, and J.-R. Grasso (2003). Mainshocks are aftershocks of conditional
628 foreshocks: How do foreshock statistical properties emerge from aftershock laws, *Journal*
629 *of Geophysical Research: Solid Earth*, 108(B1),
630 doi:<https://doi.org/10.1029/2002JB001991>.

631 Huang, H., L. Meng, R. Bürgmann, W. Wang, and K. Wang (2020). Spatio-temporal foreshock
632 evolution of the 2019 M 6.4 and M 7.1 Ridgecrest, California earthquakes, *Earth and*
633 *Planetary Science Letters*, 551, 116582, doi:<https://doi.org/10.1016/j.epsl.2020.116582>.

634 Imanishi, K., and W. L. Ellsworth (2006). Source Scaling Relationships of Microearthquakes at
635 Parkfield, CA, Determined Using the SAFOD Pilot Hole Seismic Array, in *Earthquakes:*
636 *Radiated Energy and the Physics of Faulting*, edited, pp. 81-90,
637 doi:<https://doi.org/10.1029/170GM10>.

638 Ji, L., Q. Wang, J. Xu, and J. Feng (2017). The 1996 Mw 6.6 Lijiang earthquake: Application of
639 JERS-1 SAR interferometry on a typical normal-faulting event in the northwestern Yunnan
640 rift zone, SW China, *Journal of Asian Earth Sciences*, 146, 221-232,
641 doi:<https://doi.org/10.1016/j.jseaes.2017.05.029>.

642 Johnson, P. A., B. Ferdowsi, B. M. Kaproth, M. Scuderi, M. Griffa, J. Carmeliet, R. A. Guyer, P.-
643 Y. Le Bas, D. T. Trugman, and C. Marone (2013). Acoustic emission and microslip
644 precursors to stick-slip failure in sheared granular material, *Geophysical Research Letters*,
645 40(21), 5627-5631, doi:<https://doi.org/10.1002/2013GL057848>.

646 Johnston, M. J. S., R. D. Borchardt, A. T. Linde, and M. T. Gladwin (2006). Continuous Borehole
647 Strain and Pore Pressure in the Near Field of the 28 September 2004 M 6.0 Parkfield,
648 California, Earthquake: Implications for Nucleation, Fault Response, Earthquake
649 Prediction, and Tremor, *Bulletin of the Seismological Society of America*, 96(4B), S56-S72,
650 doi:10.1785/0120050822.

651 Jones, L. M., and P. Molnar (1979). Some characteristics of foreshocks and their possible
652 relationship to earthquake prediction and premonitory slip on faults, *Journal of*
653 *Geophysical Research: Solid Earth*, 84(B7), 3596-3608,
654 doi:<https://doi.org/10.1029/JB084iB07p03596>.

655 Julian, B. R., A. D. Miller, and G. R. Foulger (1998). Non-double-couple earthquakes 1. Theory,
656 *Reviews of Geophysics*, 36(4), 525-549, doi:<https://doi.org/10.1029/98RG00716>.

657 Kato, A., K. Obara, T. Igarashi, H. Tsuruoka, S. Nakagawa, and N. Hirata (2012). Propagation of
658 Slow Slip Leading Up to the 2011 Mw9.0 Tohoku-Oki Earthquake, *Science*, 335(6069),
659 705-708, doi:10.1126/science.1215141.

660 Kato, A., and S. Nakagawa (2014). Multiple slow-slip events during a foreshock sequence of the
661 2014 Iquique, Chile Mw 8.1 earthquake, *Geophysical Research Letters*, 41(15), 5420-5427,
662 doi:<https://doi.org/10.1002/2014GL061138>.

663 Kato, A., J. i. Fukuda, S. Nakagawa, and K. Obara (2016). Foreshock migration preceding the
664 2016 Mw 7.0 Kumamoto earthquake, Japan, *Geophysical Research Letters*, 43(17), 8945-
665 8953, doi:<https://doi.org/10.1002/2016GL070079>.

666 Kato, N. (2007). Expansion of aftershock areas caused by propagating post-seismic sliding,
667 *Geophysical Journal International*, 168(2), 797-808, doi:10.1111/j.1365-
668 246X.2006.03255.x.

669 Kikuchi, M., and H. Kanamori (1982). Inversion of complex body waves, *Bulletin of the*
670 *Seismological Society of America*, 72(2), 491-506, doi:10.1785/bssa0720020491.

671 Kikuchi, M., and H. Kanamori (1986). Inversion of complex body waves-II, *Physics of the Earth*
672 *and Planetary Interiors*, 43(3), 205-222, doi:[https://doi.org/10.1016/0031-9201\(86\)90048-](https://doi.org/10.1016/0031-9201(86)90048-8)
673 [8](https://doi.org/10.1016/0031-9201(86)90048-8).

674 Kikuchi, M., and H. Kanamori (1991). Inversion of complex body waves—III, *Bulletin of the*
675 *Seismological Society of America*, 81(6), 2335-2350, doi:10.1785/bssa0810062335.

676 Kilb, D., J. Gomberg, and P. Bodin (2002). Aftershock triggering by complete Coulomb stress
677 changes, *Journal of Geophysical Research: Solid Earth*, 107(B4), ESE 2-1-ESE 2-14,
678 doi:<https://doi.org/10.1029/2001JB000202>.

679 Kim, W.-Y., H. Choi, and M. Noh (2010). The 20 January 2007 Odaesan, Korea, Earthquake
680 Sequence: Reactivation of a Buried Strike-Slip Fault?, *Bulletin of the Seismological Society*
681 *of America*, 100(3), 1120-1137, doi:10.1785/0120090069.

682 King, G. C. P., R. S. Stein, and J. Lin (1994). Static stress changes and the triggering of earthquakes,
683 *Bulletin of the Seismological Society of America*, 84(3), 935-953,
684 doi:10.1785/bssa0840030935.

685 Lei, X., Z. Wang, S. Ma, and C. He (2021). A preliminary study on the characteristics and
686 mechanism of the May 2021 Ms6.4 Yangbi earthquake sequence, Yunnan, China, *Acta*
687 *Seismologica Sinica*, 43(3), 261, doi:10.11939/jass.20210100.

688 Li, C., X. Shan, G. Zhang, C. Zhao, W. Gong, and Y. Zhang (2022). Slip Kinematics of the 2021
689 Yangbi Earthquake: Fore-Main-Aftershock Sequence Rupture along an Unknown
690 Secondary Fault of the Weixi-Qiaohou Fault, *Seismological Research Letters*,
691 doi:10.1785/0220210220.

692 Lin, G. (2020). Spatiotemporal variations of in situ Vp/Vs ratio within the Salton Sea Geothermal
693 Field, southern California, *Geothermics*, 84, 101740,
694 doi:<https://doi.org/10.1016/j.geothermics.2019.101740>.

695 Lin, J., and R. S. Stein (2004). Stress triggering in thrust and subduction earthquakes and stress
696 interaction between the southern San Andreas and nearby thrust and strike-slip faults,
697 *Journal of Geophysical Research: Solid Earth*, 109(B2),
698 doi:<https://doi.org/10.1029/2003JB002607>.

699 Liu, X., W. Xu, Z. He, L. Fang, and Z. Chen (2022). Aseismic slip and cascade triggering process
700 of foreshocks leading to the 2021 Mw 6.1 Yangbi Earthquake, *Seismological Research*
701 *Letters (in press)*.

702 Liu, Y., H. Yao, H. Zhang, and H. Fang (2021). The Community Velocity Model V.1.0 of
703 Southwest China, Constructed from Joint Body- and Surface-Wave Travel-Time
704 Tomography, *Seismological Research Letters*, doi:10.1785/0220200318.

705 López-Comino, J. A., and S. Cesca (2018). Source Complexity of an Injection Induced Event: The
706 2016 Mw 5.1 Fairview, Oklahoma Earthquake, *Geophysical Research Letters*, 45(9),
707 4025-4032, doi:<https://doi.org/10.1029/2018GL077631>.

708 Madariaga, R. (1976). Dynamics of an expanding circular fault, *Bulletin of the Seismological*
709 *Society of America*, 66(3), 639-666.

710 McLaskey, G. C. (2019). Earthquake Initiation From Laboratory Observations and Implications
711 for Foreshocks, *Journal of Geophysical Research: Solid Earth*, 124(12), 12882-12904,
712 doi:<https://doi.org/10.1029/2019JB018363>.

713 Mendoza, M. M., A. Ghosh, M. S. Karplus, S. L. Klemperer, S. N. Sapkota, L. B. Adhikari, and
714 A. Velasco (2019). Duplex in the Main Himalayan Thrust illuminated by aftershocks of
715 the 2015 Mw 7.8 Gorkha earthquake, *Nature Geoscience*, 12(12), 1018-1022,
716 doi:10.1038/s41561-019-0474-8.

717 Meng, H., and W. Fan (2021). Immediate Foreshocks Indicating Cascading Rupture Developments
718 for 527 M 0.9 to 5.4 Ridgecrest Earthquakes, *Geophysical Research Letters*, 48(19),
719 e2021GL095704, doi:<https://doi.org/10.1029/2021GL095704>.

720 Meng, Q., S. Ni, and Z. Peng (2021). Complex Source Behaviors and Spatiotemporal Evolution
721 of Seismicity During the 2015–2016 Earthquake Sequence in Cushing, Oklahoma, *Journal*
722 *of Geophysical Research: Solid Earth*, 126(6), e2021JB022168,
723 doi:<https://doi.org/10.1029/2021JB022168>.

724 Meng, X., and Z. Peng (2015). Increasing lengths of aftershock zones with depths of moderate-
725 size earthquakes on the San Jacinto Fault suggests triggering of deep creep in the middle
726 crust, *Geophysical Journal International*, 204(1), 250-261, doi:10.1093/gji/ggv445.

727 Mignan, A. (2014). The debate on the prognostic value of earthquake foreshocks: A meta-analysis,
728 *Scientific Reports*, 4(1), 4099, doi:10.1038/srep04099.

729 Parsons, T., and A. A. Velasco (2009). On near-source earthquake triggering, *Journal of*
730 *Geophysical Research: Solid Earth*, 114(B10), doi:<https://doi.org/10.1029/2008JB006277>.

731

732 Peng, Z., and P. Zhao (2009). Migration of early aftershocks following the 2004 Parkfield
733 earthquake, *Nature Geoscience*, 2(12), 877-881, doi:10.1038/ngeo697.

734 Perfettini, H., and J.-P. Avouac (2004). Postseismic relaxation driven by brittle creep: A possible
735 mechanism to reconcile geodetic measurements and the decay rate of aftershocks,
736 application to the Chi-Chi earthquake, Taiwan, *Journal of Geophysical Research: Solid*
737 *Earth*, 109(B2), doi:<https://doi.org/10.1029/2003JB002488>.

738 Prieto, G. A., R. L. Parker, and F. L. Vernon III (2009). A Fortran 90 library for multitaper
739 spectrum analysis, *Computers & Geosciences*, 35(8), 1701-1710,
740 doi:<https://doi.org/10.1016/j.cageo.2008.06.007>.

741 Roeloffs, E. A. (2006). Evidence for Aseismic Deformation Rate Changes Prior to Earthquakes,
742 *Annual Review of Earth and Planetary Sciences*, 34(1), 591-627,
743 doi:10.1146/annurev.earth.34.031405.124947.

744 Ross, Z. E., and Y. Ben-Zion (2016). Toward reliable automated estimates of earthquake source
745 properties from body wave spectra, *Journal of Geophysical Research: Solid Earth*, 121(6),
746 4390-4407, doi:<https://doi.org/10.1002/2016JB013003>.

747 Ruiz, S., M. Metois, A. Fuenzalida, J. Ruiz, F. Leyton, R. Grandin, C. Vigny, R. Madariaga, and
748 J. Campos (2014). Intense foreshocks and a slow slip event preceded the 2014 Iquique
749 *M_w 8.1 earthquake*, *Science*, 345(6201), 1165-1169,
750 doi:10.1126/science.1256074.

751 Ruiz, S., et al. (2017). Nucleation Phase and Dynamic Inversion of the Mw 6.9 Valparaíso 2017
752 Earthquake in Central Chile, *Geophysical Research Letters*, 44(20), 10,290-210,297,
753 doi:<https://doi.org/10.1002/2017GL075675>.

754 Shelly, D. R. (2020). A High-Resolution Seismic Catalog for the Initial 2019 Ridgecrest
755 Earthquake Sequence: Foreshocks, Aftershocks, and Faulting Complexity, *Seismological*
756 *Research Letters*, doi:10.1785/0220190309.

757 Shen, Z.-K., J. Lü, M. Wang, and R. Bürgmann (2005). Contemporary crustal deformation around
758 the southeast borderland of the Tibetan Plateau, *Journal of Geophysical Research: Solid*
759 *Earth*, 110(B11), doi:10.1029/2004jb003421.

760 Steacy, S., J. Gomberg, and M. Cocco (2005). Introduction to special section: Stress transfer,
761 earthquake triggering, and time-dependent seismic hazard, *Journal of Geophysical*
762 *Research: Solid Earth*, 110(B5), doi:<https://doi.org/10.1029/2005JB003692>.

763 Sun, Q., Z. Guo, S. Pei, Y. V. Fu, and Y. J. Chen (2022). Fluids Triggered the 2021 Mw 6.1 Yangbi
764 Earthquake at an Unmapped Fault: Implications for the Tectonics at the Northern End of
765 the Red River Fault, *Seismological Research Letters*, 93(2A), 666-679,
766 doi:10.1785/0220210227.

767 Tape, C., S. Holtkamp, V. Silwal, J. Hawthorne, Y. Kaneko, J. P. Ampuero, C. Ji, N. Ruppert, K.
768 Smith, and M. E. West (2018). Earthquake nucleation and fault slip complexity in the lower
769 crust of central Alaska, *Nature Geoscience*, 11(7), 536-541, doi:10.1038/s41561-018-
770 0144-2.

771 Toda, S., R. S. Stein, K. Richards-Dinger, and S. B. Bozkurt (2005). Forecasting the evolution of
772 seismicity in southern California: Animations built on earthquake stress transfer, *Journal*
773 *of Geophysical Research: Solid Earth*, 110(B5),
774 doi:<https://doi.org/10.1029/2004JB003415>.

775 Uchida, N., T. Matsuzawa, W. L. Ellsworth, K. Imanishi, T. Okada, and A. Hasegawa (2007).
776 Source parameters of a M4.8 and its accompanying repeating earthquakes off Kamaishi,
777 NE Japan: Implications for the hierarchical structure of asperities and earthquake cycle,
778 *Geophysical Research Letters*, 34(20), doi:<https://doi.org/10.1029/2007GL031263>.

779 Waldhauser, F. (2001). hypoDD--A program to compute double-difference hypocenter locations,
780 *U.S. Geological Survey Open-File Report 01-113*, 25 pp.

781 Wang, G., Z. Wu, G. Peng, Z. Liu, R. Luo, X. Huang, and H. Chen (2021). Seismogenic fault and
782 its rupture characteristics of 21 May, 2021 Yangbi Ms6.4 earthquake: analysis results from
783 relocation of earthquake sequence, *Journal of Geomechanics (in Chinese)*, 27(4), 1-22.

784 Wang, K., Q.-F. Chen, S. Sun, and A. Wang (2006). Predicting the 1975 Haicheng Earthquake,
785 *Bulletin of the Seismological Society of America*, 96(3), 757-795, doi:10.1785/0120050191.
786

787 Wang, W., J. He, X. Wang, Y. Zhou, J. Hao, L. Zhao, and Z. Yao (2022). Rupture process models
788 of the Yangbi and Maduo earthquakes that struck the eastern Tibetan Plateau in May 2021,
789 *Science Bulletin*, 67(5), 466-469, doi:<https://doi.org/10.1016/j.scib.2021.11.009>.

790 Wu, Q., X. Chen, and R. E. Abercrombie (2019). Source Complexity of the 2015 Mw 4.0 Guthrie,
791 Oklahoma Earthquake, *Geophysical Research Letters*, 46(9), 4674-4684,
792 doi:<https://doi.org/10.1029/2019GL082690>.

793 Xu, S., B. Wang, L. M. Jones, X. Ma, and P. Shen (1982). The foreshock sequence of haicheng
794 earthquake and earthquake swarm—the use of foreshock sequences in earthquake
795 prediction, *Tectonophysics*, 85(1), 91-105, doi:[https://doi.org/10.1016/0040-1951\(82\)90079-8](https://doi.org/10.1016/0040-1951(82)90079-8).

797 Yang, Z., J. Liu, X.-M. Zhang, W. Deng, G. Du, and X. Wu (2021). A preliminary report of the
798 Yangbi, Yunnan, Ms6.4 earthquake of May 21, 2021, *Earth and Planetary Physics*, 5(4),
799 1-3, doi:10.26464/epp2021036.

800 Yao, D., Y. Huang, Z. Peng, and R. R. Castro (2020). Detailed Investigation of the Foreshock
801 Sequence of the 2010 Mw7.2 El Mayor-Cucapah Earthquake, *Journal of Geophysical*
802 *Research: Solid Earth*, 125(6), e2019JB019076,
803 doi:<https://doi.org/10.1029/2019JB019076>.

804 Yoon, C. E., N. Yoshimitsu, W. L. Ellsworth, and G. C. Beroza (2019). Foreshocks and Mainshock
805 Nucleation of the 1999 Mw 7.1 Hector Mine, California, Earthquake, *Journal of*
806 *Geophysical Research: Solid Earth*, 124(2), 1569-1582,
807 doi:<https://doi.org/10.1029/2018JB016383>.

808 Yue, H., Z. E. Ross, C. Liang, S. Michel, H. Fattahi, E. Fielding, A. Moore, Z. Liu, and B. Jia
809 (2017). The 2016 Kumamoto Mw = 7.0 Earthquake: A Significant Event in a Fault–
810 Volcano System, *Journal of Geophysical Research: Solid Earth*, 122(11), 9166-9183,
811 doi:<https://doi.org/10.1002/2017JB014525>.

812 Yue, H., and T. Lay (2020). Resolving Complicated Faulting Process Using Multi-Point-Source
813 Representation: Iterative Inversion Algorithm Improvement and Application to Recent
814 Complex Earthquakes, *Journal of Geophysical Research: Solid Earth*, 125(2),
815 e2019JB018601, doi:<https://doi.org/10.1029/2019JB018601>.

816 Yue, H., J. Sun, M. Wang, Z. Shen, M. Li, L. Xue, W. Lu, Y. Zhou, C. Ren, and T. Lay (2021).
817 The 2019 Ridgecrest, California earthquake sequence: Evolution of seismic and aseismic
818 slip on an orthogonal fault system, *Earth and Planetary Science Letters*, 570, 117066,
819 doi:<https://doi.org/10.1016/j.epsl.2021.117066>.

820 Yun, N., S. Zhou, H. Yang, H. Yue, and L. Zhao (2019). Automated Detection of Dynamic
821 Earthquake Triggering by the High-Frequency Power Integral Ratio, *Geophysical*
822 *Research Letters*, 46(22), 12977-12985, doi:<https://doi.org/10.1029/2019GL083913>.

823 Zhang, P., Q. Deng, G. Zhang, J. Ma, W. Gan, W. Min, F. Mao, and Q. Wang (2003). Active
824 tectonic blocks and strong earthquakes in the continent of China, *Science in China Series*
825 *D: Earth Sciences*, 46(2), 13-24, doi:10.1360/03dz0002.

826 Zhang, Y., Y. An, F. Long, G. Zhu, M. Qin, Y. Zhong, Q. Xu, and H. Yang (2021). Short-Term
827 Foreshock and Aftershock Patterns of the 2021 Ms 6.4 Yangbi Earthquake Sequence,
828 *Seismological Research Letters*, 93(1), 21-32, doi:10.1785/0220210154.

- 829 Zhou, Y., H. Yue, Q. Kong, and S. Zhou (2019). Hybrid Event Detection and Phase-Picking
830 Algorithm Using Convolutional and Recurrent Neural Networks, *Seismological Research*
831 *Letters*, 90(3), 1079-1087, doi:10.1785/0220180319.
- 832 Zhou, Y., A. Ghosh, L. Fang, H. Yue, S. Zhou, and Y. Su (2021a). A High-Resolution Seismic
833 Catalog for the 2021 Ms6.4/Mw6.1 YangBi Earthquake Sequence, Yunnan, China:
834 Application of AI picker and Matched Filter, *Earthquake Science*, 34(5), 390-398,
835 doi:10.29382/eqs-2021-0031.
- 836 Zhou, Y., H. Yue, L. Fang, S. Zhou, L. Zhao, and A. Ghosh (2021b). An Earthquake Detection
837 and Location Architecture for Continuous Seismograms: Phase Picking, Association,
838 Location, and Matched Filter (PALM), *Seismological Research Letters*, 93(1), 413-425,
839 doi:10.1785/0220210111.
- 840 Zhu, L., and L. A. Rivera (2002). A note on the dynamic and static displacements from a point
841 source in multilayered media, *Geophysical Journal International*, 148(3), 619-627,
842 doi:10.1046/j.1365-246X.2002.01610.x.
- 843 Ziv, A., and A. M. Rubin (2000). Static stress transfer and earthquake triggering: No lower
844 threshold in sight?, *Journal of Geophysical Research: Solid Earth*, 105(B6), 13631-13642,
845 doi:<https://doi.org/10.1029/2000JB900081>.
- 846

Seismological Characterization of the 2021 Yangbi Foreshock-Mainshock Sequence, Yunnan, China: More than a Triggered Cascade

Yijian Zhou^{1*}, Chunmei Ren², Abhijit Ghosh¹, Haoran Meng³, Lihua Fang^{4*}, Han Yue², Shiyong Zhou², and Youjin Su⁵

¹Department of Earth and Planetary Sciences, University of California, Riverside, California, USA

²Institute of Theoretical and Applied Geophysics, Peking University, Beijing, China.

³Southern University of Science and Technology, Guangdong, China

⁴Institute of Geophysics, China Earthquake Administration, Beijing, China

⁵Yunnan Earthquake Agency, Yunnan, China

Contents of this file

Text S1
Figures S1 to S17
Table S1 to S2

Introduction

This supporting information provides additional details on the multi-point-source inversion process, source spectrum analysis, and Coulomb stress modelling.

Text S1

Tests on MPS inversion process for the largest foreshock. We demonstrate the necessity of using two subevents for the largest foreshock by presenting the inversion result with different search windows. First, we tried single subevent to fit the observations. We set the time window to 0-10s, and results show that synthetic waveforms can fit only the initial seismic phase and first 1-2 wiggles, yet the remaining unfitted waveforms resembles another seismic event (Figure S14). Instead, when the time window is given posterior, from the initiation 3-10s, the synthetics are coherent with major peaks, while the initial phase becomes reversed (figure S13), resulting in an absolutely opposite mechanism (i.e. left-lateral). Therefore, we add another subevent to simulate the rupture process of the foreshock on the basis of the solution exhibit in figure S10a.

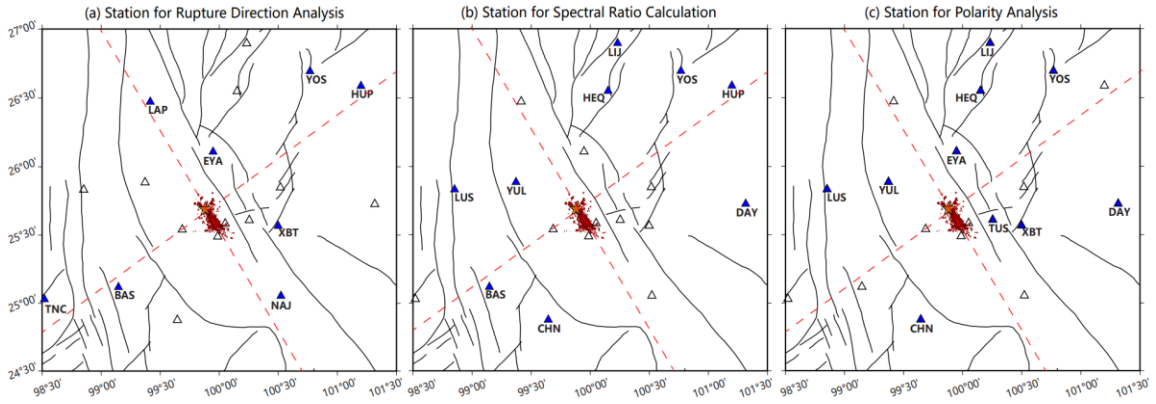


Figure S1. Stations used for different analysis. (a), (b), and (c) plot stations for rupture direction analysis, spectral ration calculation, and for polarity analysis, respectively. The blue triangles with the names annotated is the selected stations, and the hollow black triangles are stations not selected. The red dashed lines mark the nodal plane direction of the mainshock.

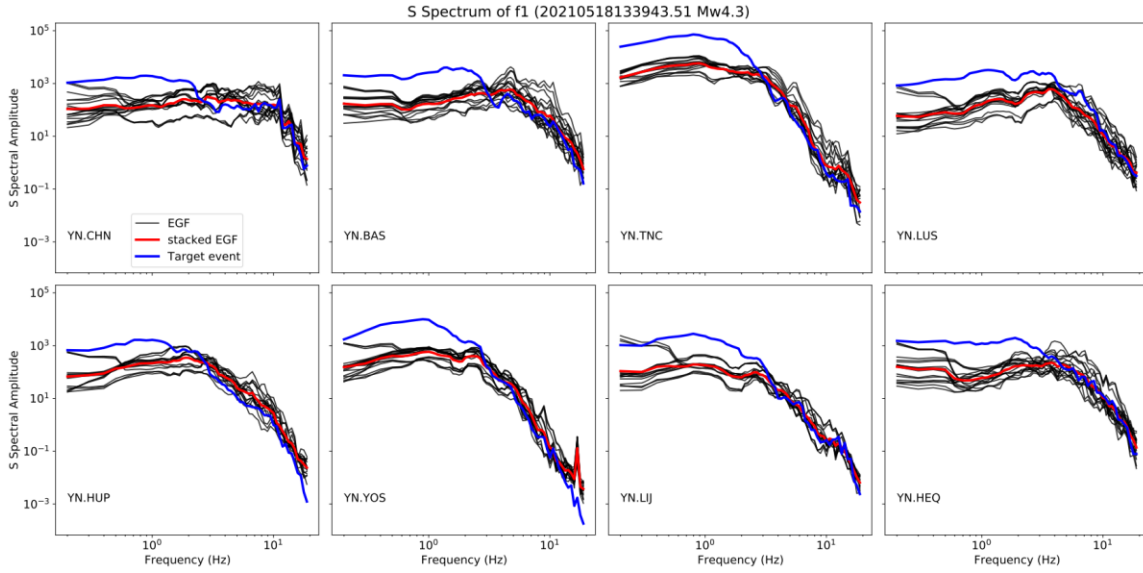


Figure S2. Spectral amplitudes of *f1*. The spectral amplitude of EGF, stacked EGF, and target events are plotted in black, red, and blue lines, respectively. Each subplot shows results on one station.

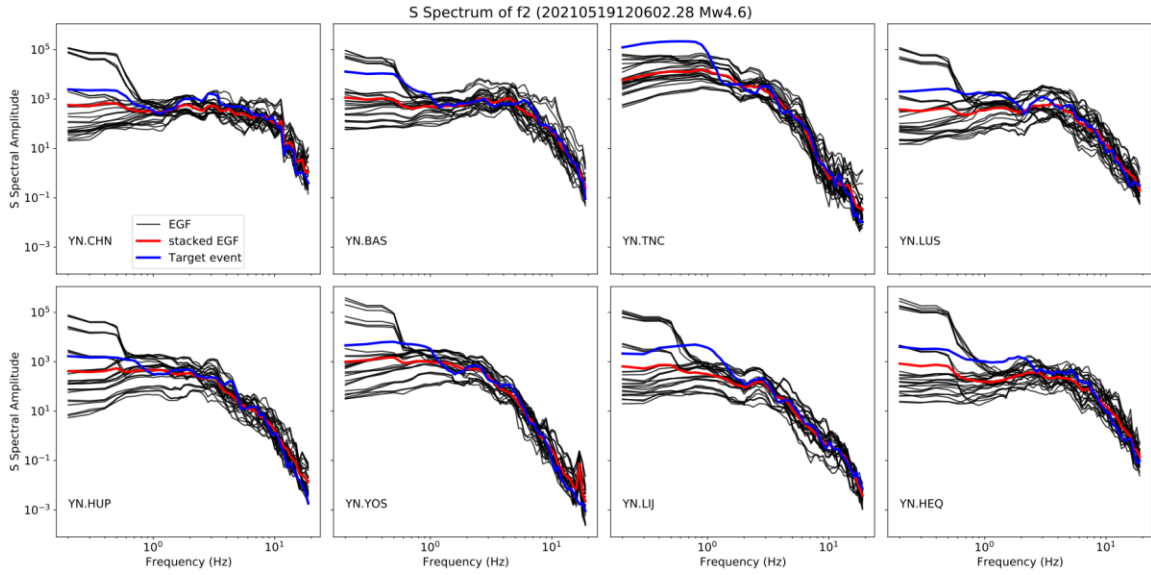


Figure S3. Spectral amplitudes of f_2 . The markers have the same meaning as that in Figure S2.

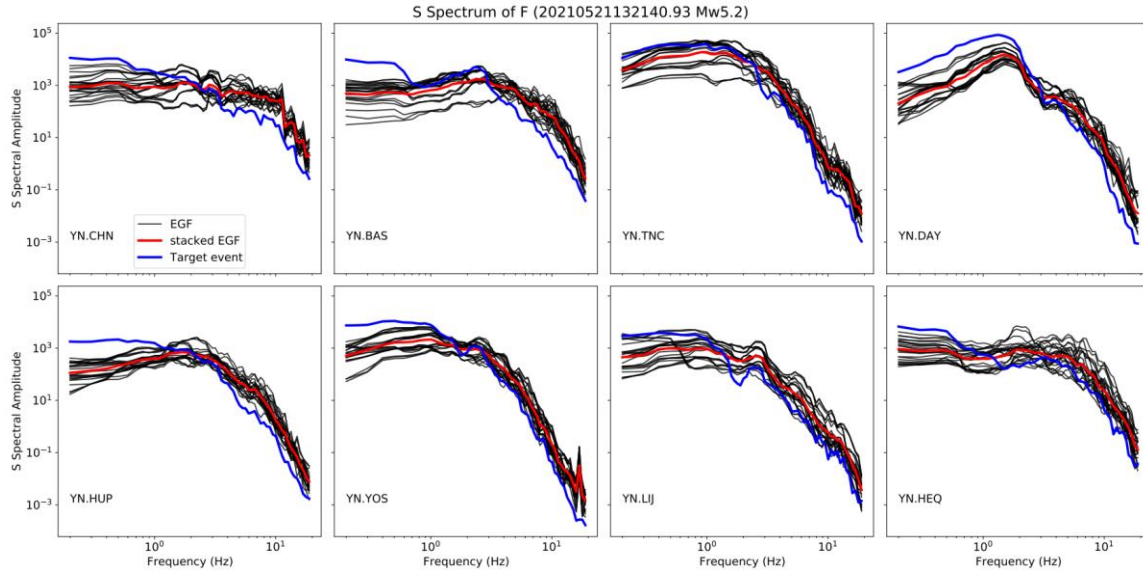


Figure S4. Spectral amplitudes of *F1*. The markers have the same meaning as that in Figure S2.

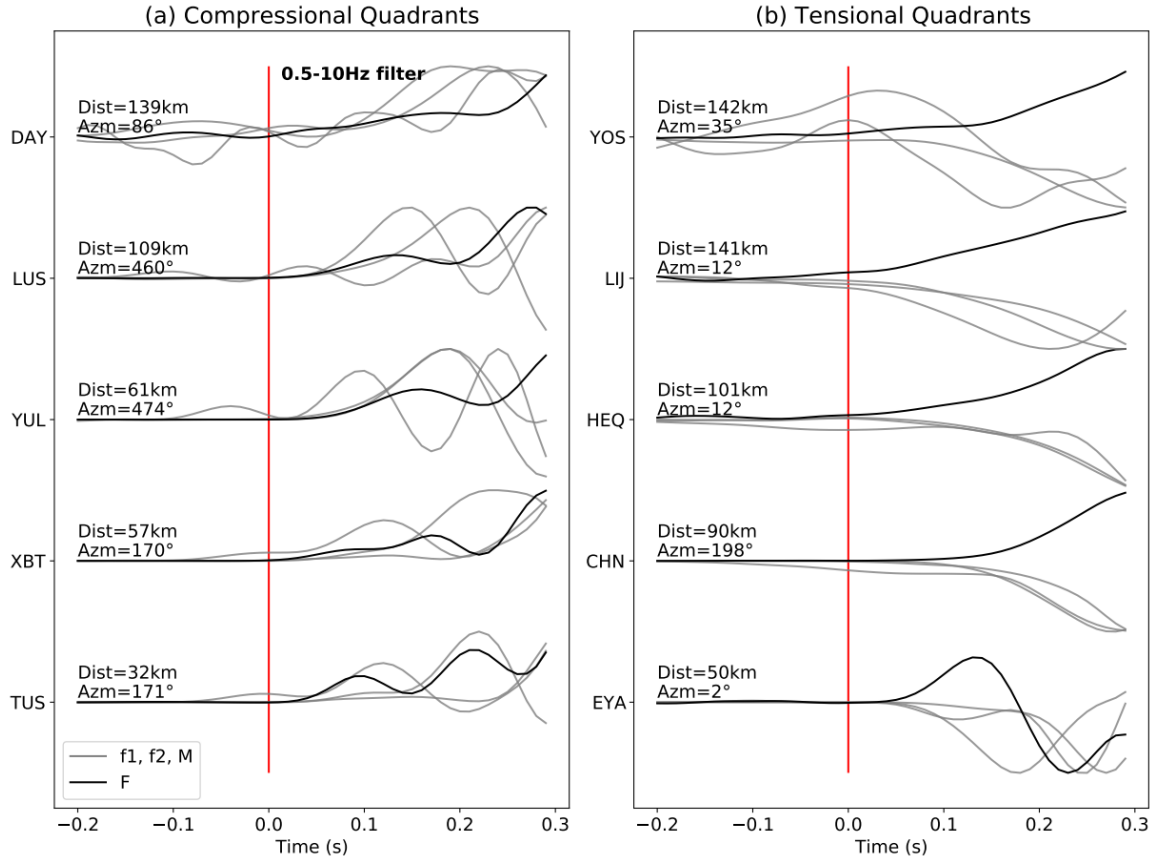


Figure S5. Polarization of *FI* records. (a) & (b) plot stations in the compressional and tensional quadrants, respectively. The gray lines plot P wave of major events on *Fault_M*, i.e. *f1*, *f2*, and *M*; black lines plot that of *FI*. The P-wave is obtained by first bandpass filter a 30-s window by 0.5-10Hz, and slice to a zoom-in window.

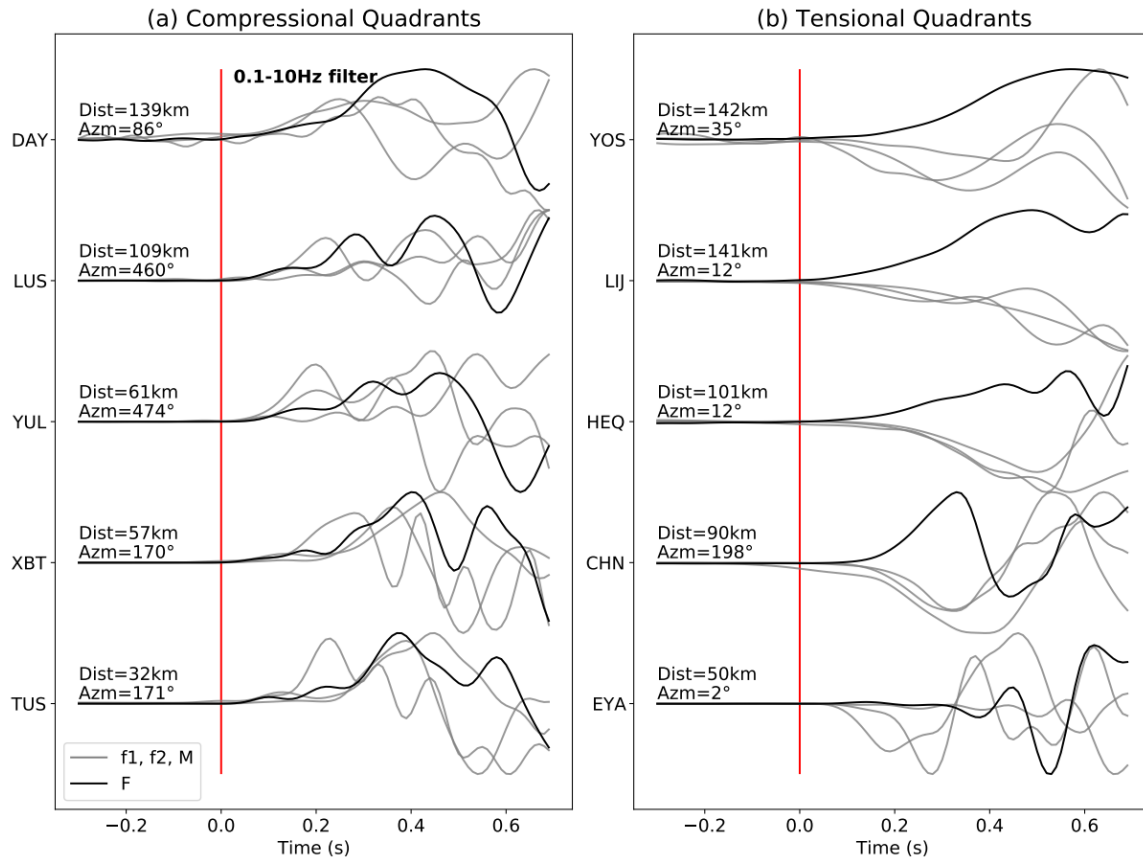


Figure S6. Same as Figure S5, but with longer window and lower frequency band.

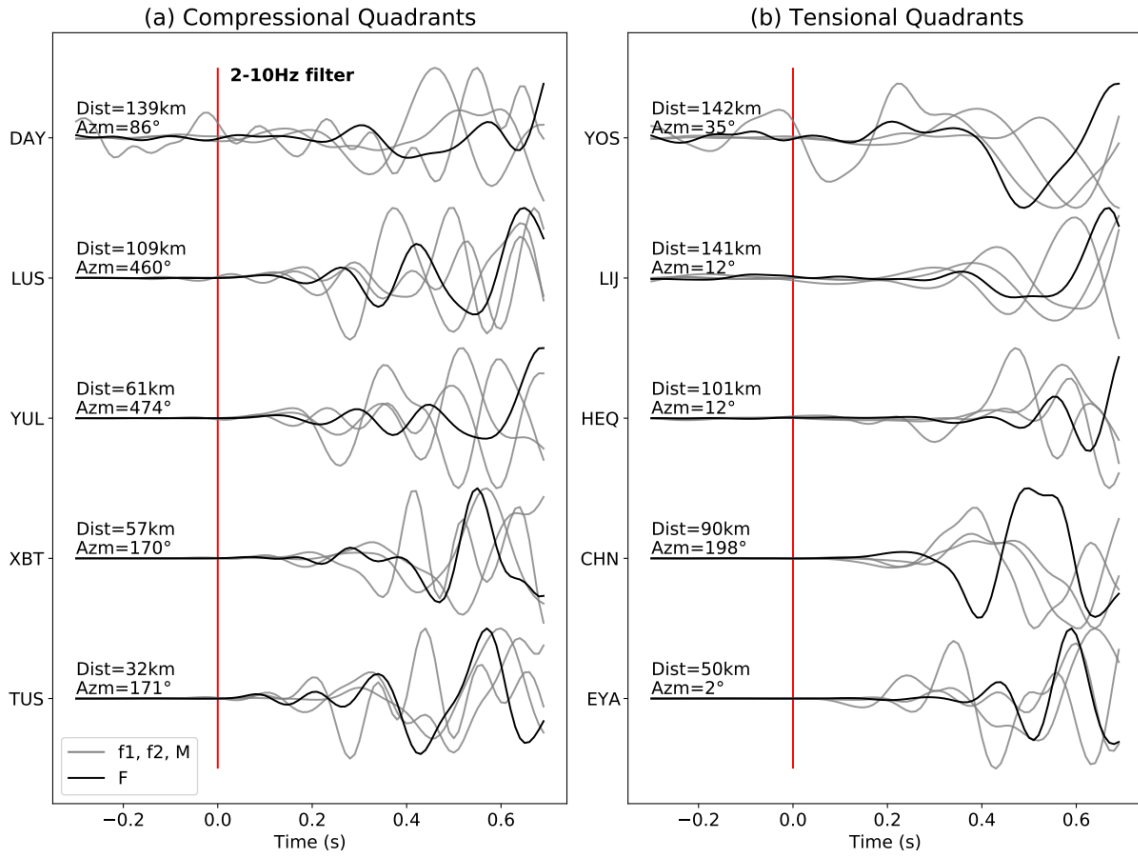


Figure S7. Same as Figure S5, but with longer window and higher frequency band.

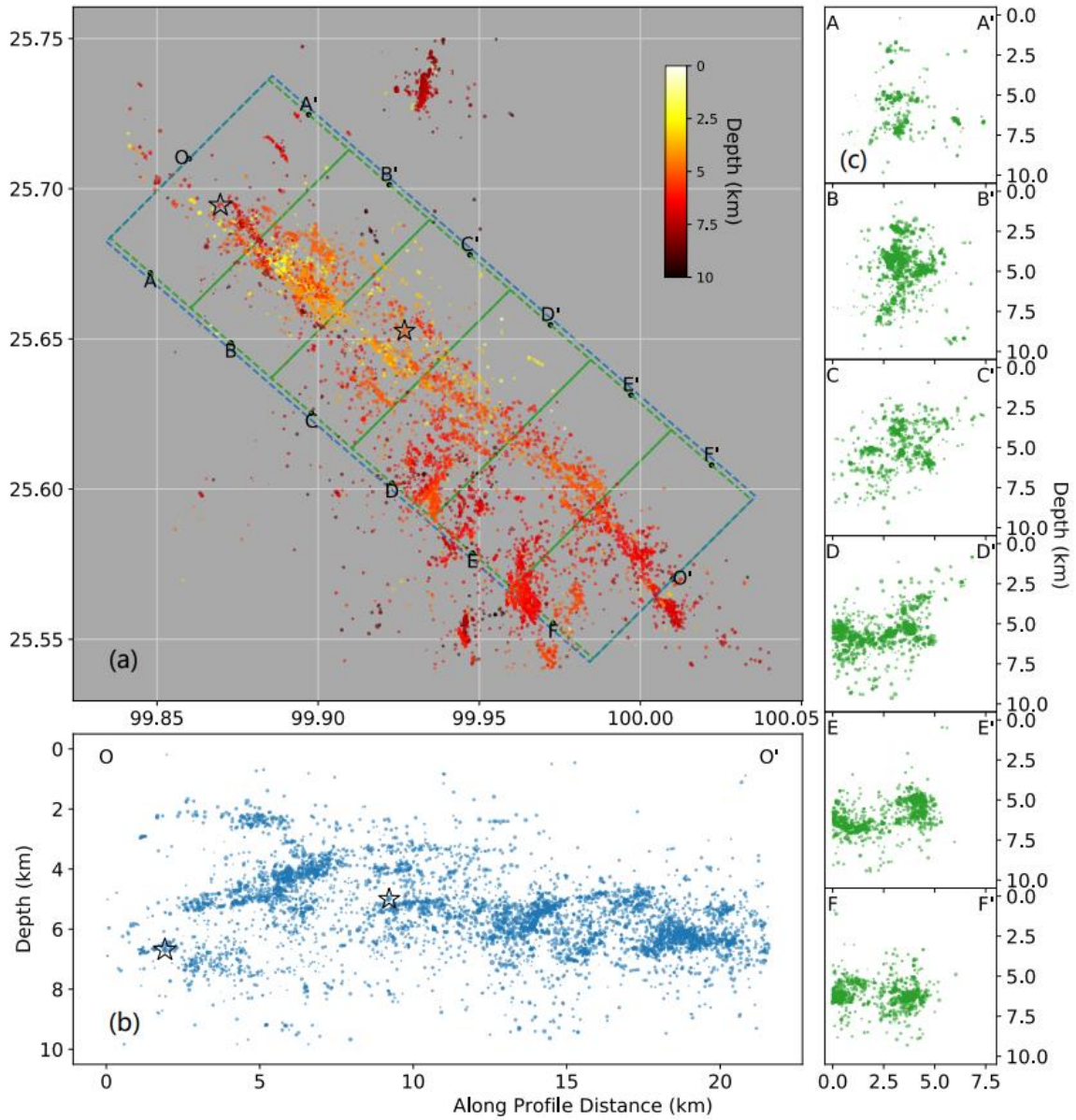


Figure S8. Distribution of Yangbi aftershocks from 17th May to 28th May. (a), (b), and (c) show map view, along-strike cross-section, and fault-vertical cross-sections, respectively. seismic events are plot in dots with the size scaled by its magnitude. The hypocentral depth in (a) is represented by color. Location of the mainshock *M* and the largest foreshock *F* is plotted in hollow stars.

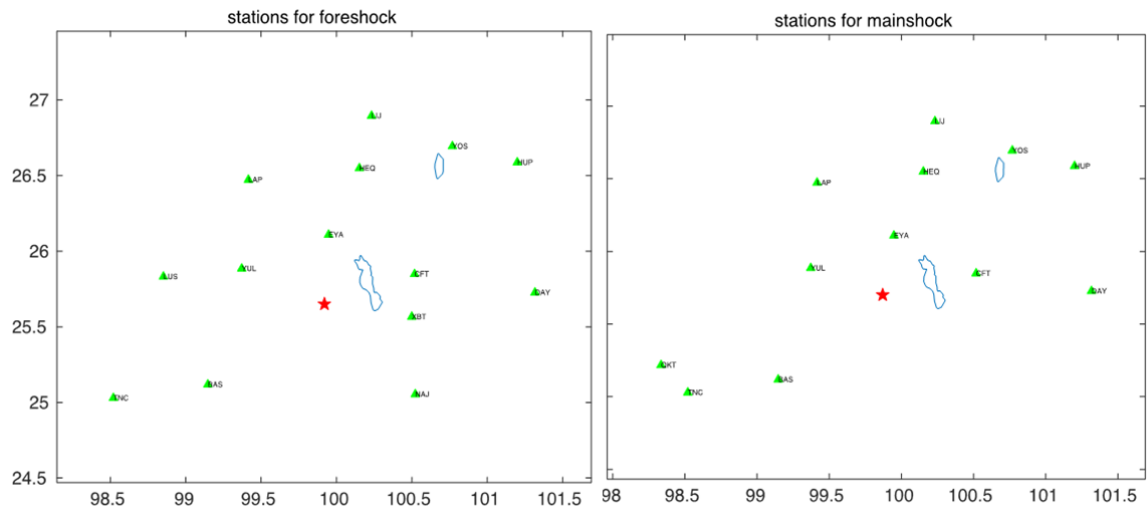


Figure S9. Stations for MPS inversion.

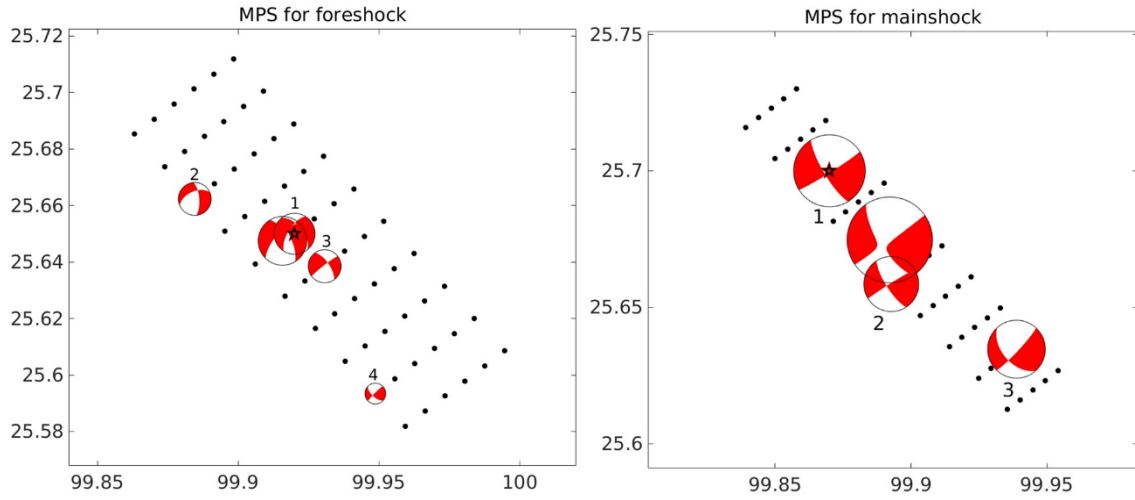


Figure S10. MPS inversion result. The black dots are the preset mesh grids. The black star marks the epicenter.

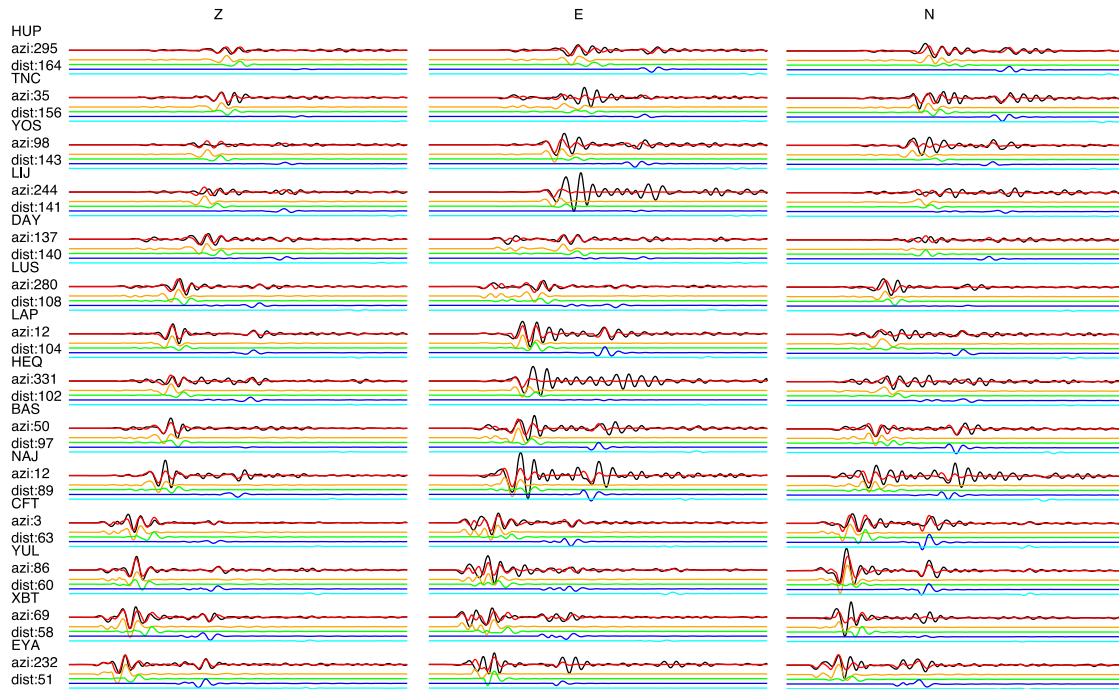


Figure S11. MPS waveform fitting for the largest foreshock. The black and red lines are the observation and predicted waveforms. The waveforms below in other colors are that predicted by each subevents.

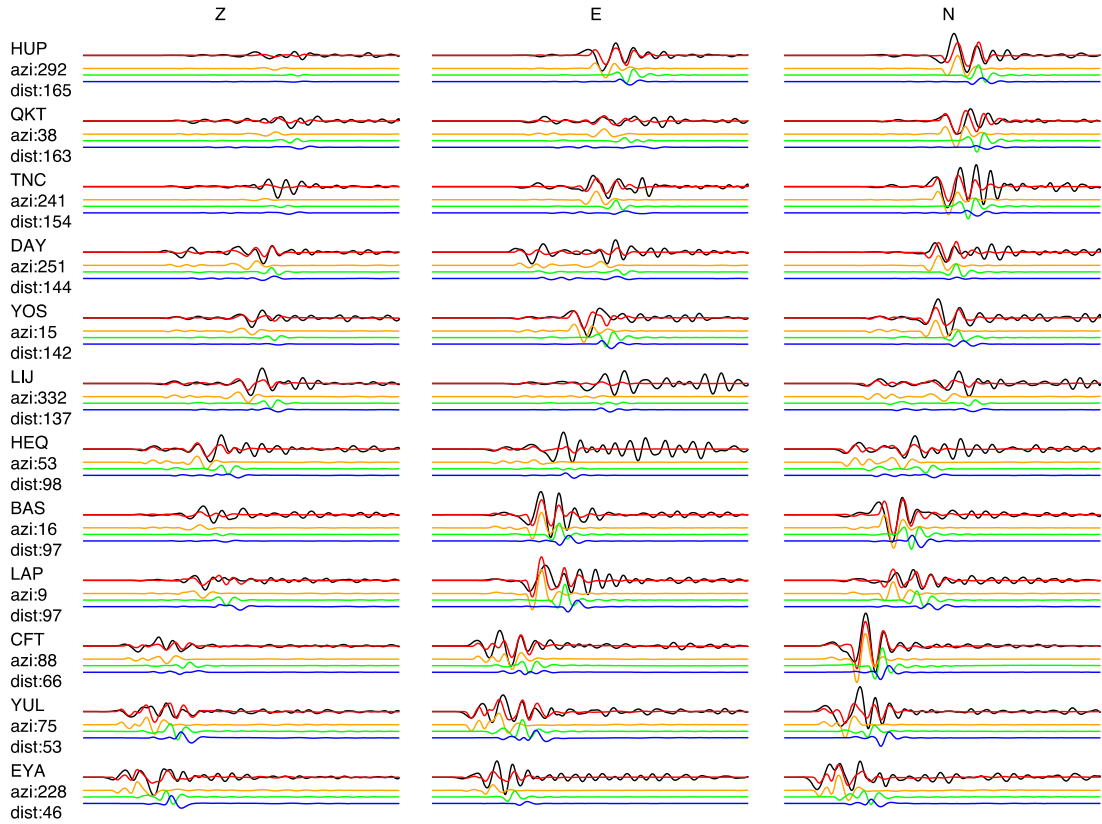


Figure S12. MPS waveform fitting for the mainshock. The symbols have the same meaning with Figure S11.

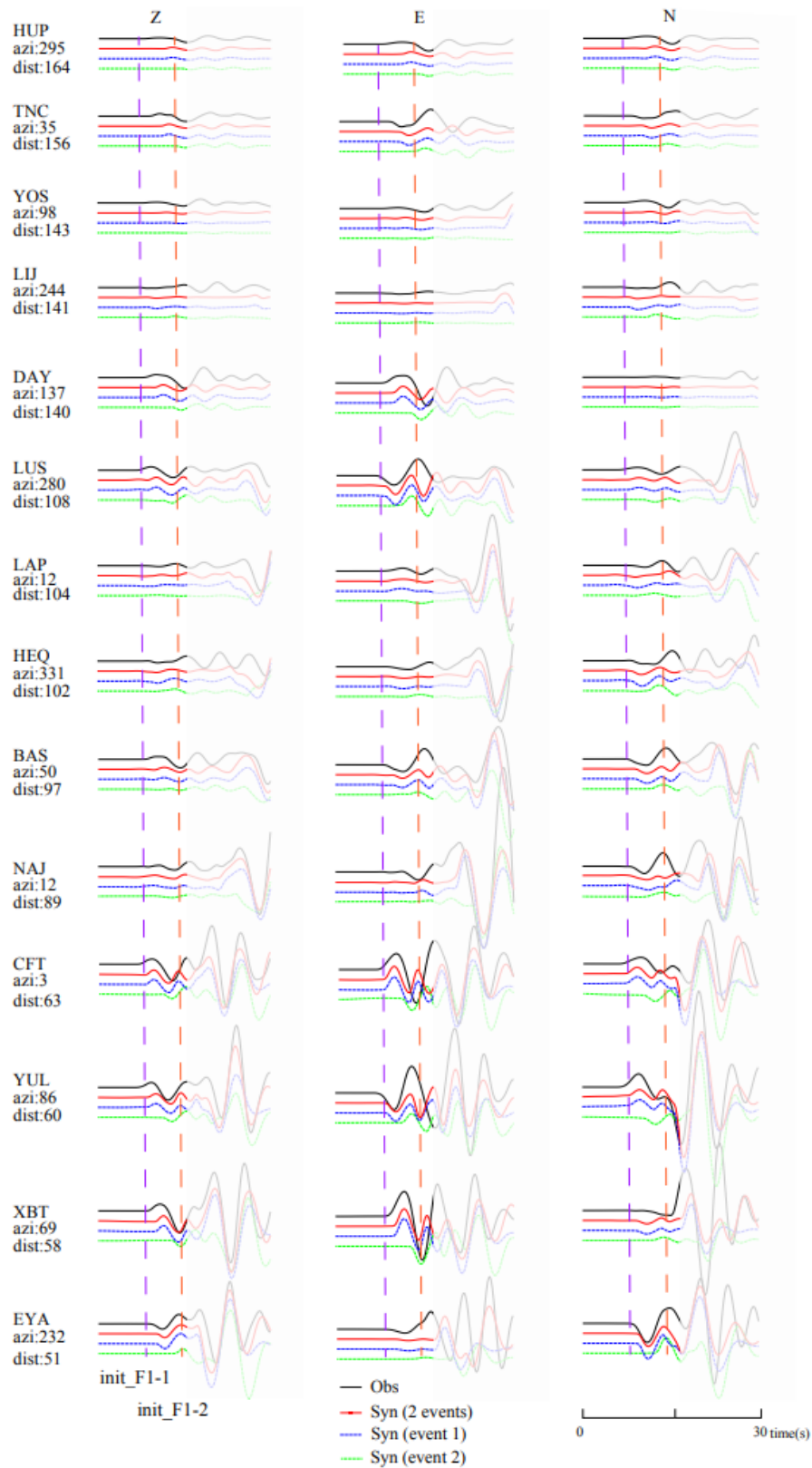


Figure S13. Comparison of MPS inversion result for FI with different choices of searching window. The purple and red vertical dashed lines plot the P arrival of FI_1 and FI_2 .

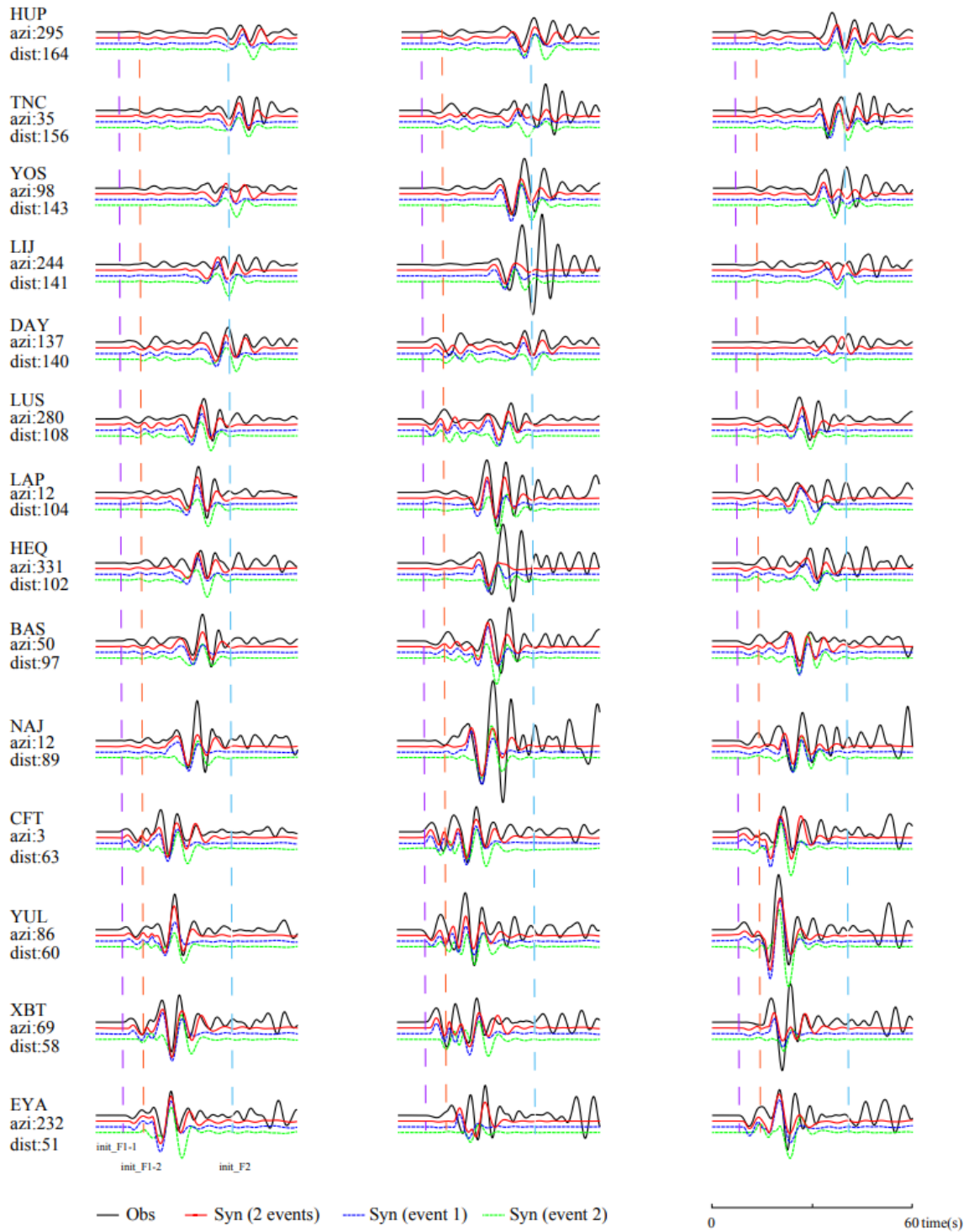


Figure S14. Same as Figure S13, but show longer window.

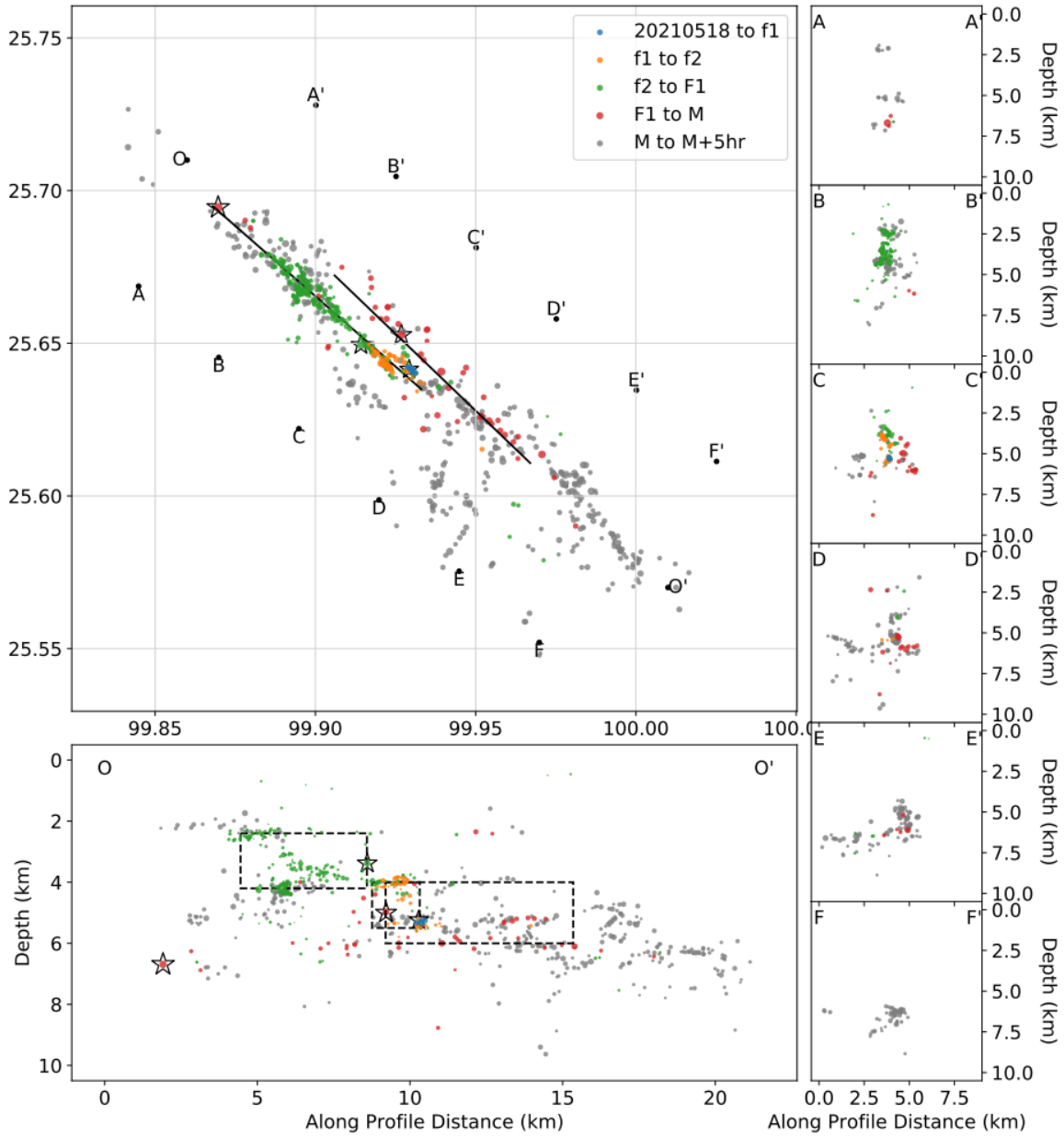


Figure S15. Fault model for a pure-unilateral $F1$ rupture. The symbols have the same meaning as in Figure 7.

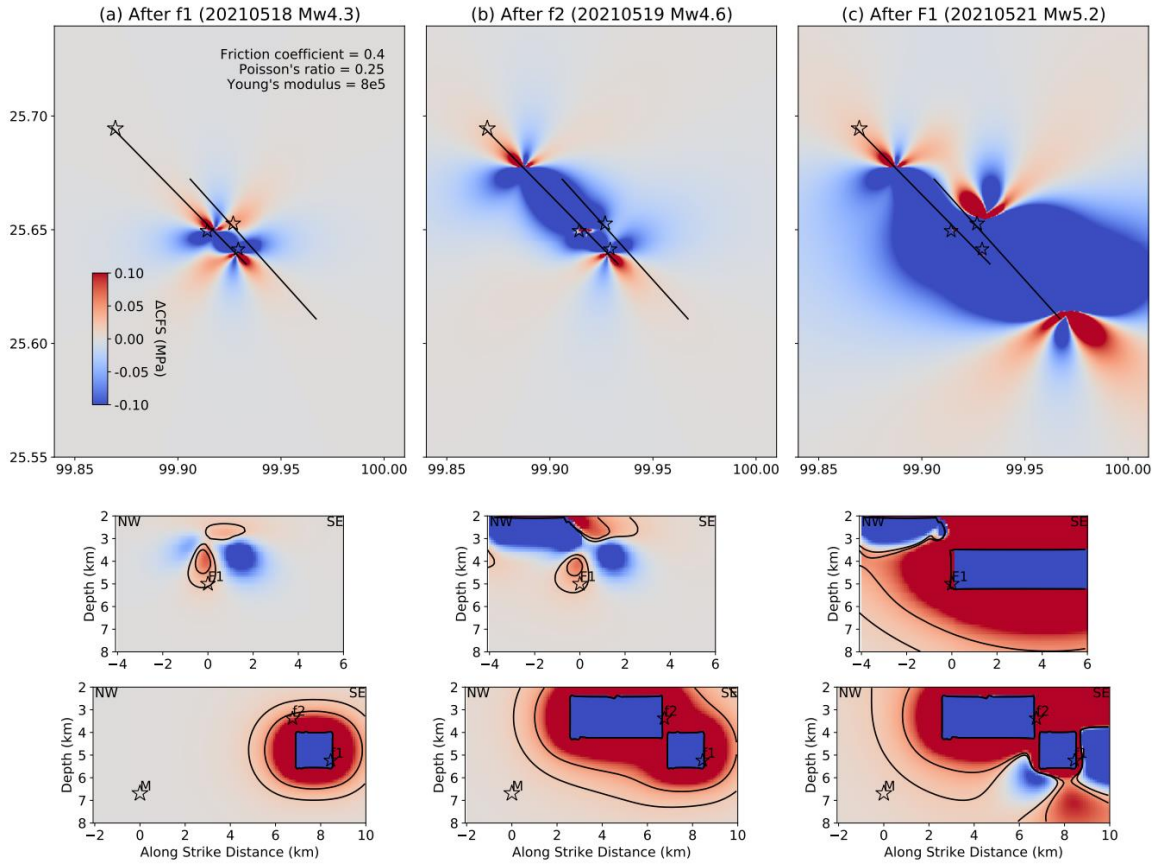


Figure S16. Coulomb stress evolution with $F1$ as a purely uni-lateral rupture. The symbols have the same meaning as in Figure 8.

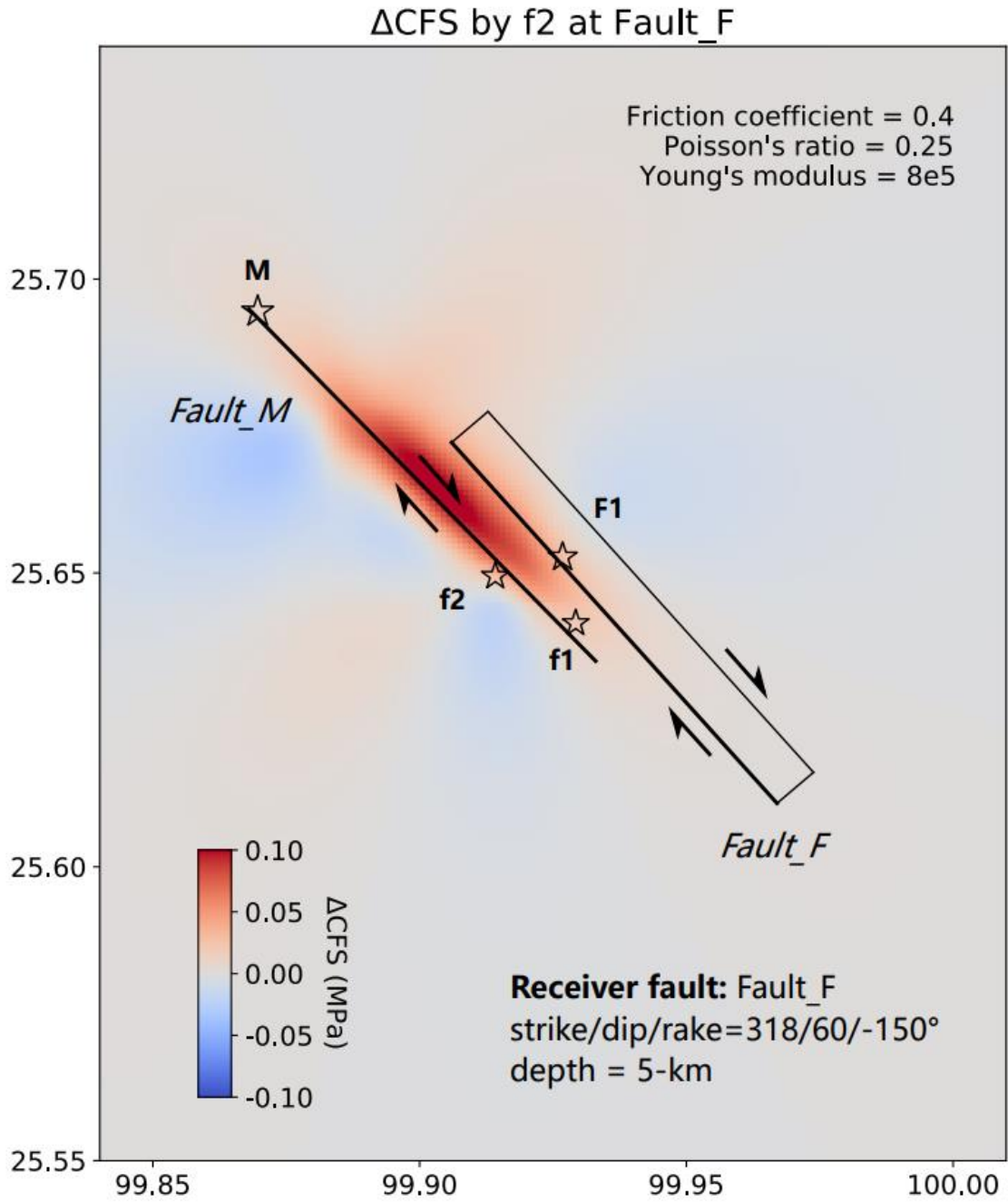


Figure S17. Coulomb stress change induced by f_2 with *Fault_F* as the receiver fault at a depth of 5-km.

Table S1. MPS result of the largest foreshock

Subevent	Time(s)	Location(lat/lon/dep)	Mechanism(strike/dip/rake)		M_w
1	0.0	25.65/99.92/15.0	320/56/-148	211/63/-37	5.1
2	5.2	25.66/99.88/13.5	354/67/-138	246/52/-29	4.8
Sum 1&2	2.2	25.65/99.91/14.5	332/58/-142	220/58/-38	5.1
3	31.2	25.64/99.93/15	324/67/-174	232/84/-22	4.9
4	69.2	25.59/99.95/13.5	224/84/26	132/63/174	4.4
Sum all	12.1	25.65/99.92/14.6	328/62/-151	224/64/-30	5.2

Table S2. MPS result of the mainshock

Subevent	Time(s)	Location(lat/lon/dep)	Mechanism(strike/dip/rake)		M_w
1	0.0	25.70/99.87/17.0	148/77/-175	57/85/-12	5.7
2	5.9	25.66/99.89/7.1	237/87/15	147/74/177	5.4
3	8.4	25.63/99.94/8.4	138/51/-171	43/83/-39	5.5
Sum	4.4	25.67/99.89/16.1	145/70/-177	55/87/-19	5.8